JOURNAL OF PETROLOGY | VOLUME 48 | NUMBER 8 | PAGES 1513–1542 | 2007 | doi:10.1093/petrology/egm028

Magma Genesis and Mantle Dynamics at the Harrat Ash Shamah Volcanic Field (Southern Syria)

M.-S. KRIENITZ[1]*, K. M. HAASE[1]†, K. MEZGER[2] AND M. A. SHAIKH-MASHAIL[3]

[1]INSTITUT FÜR GEOWISSENSCHAFTEN DER UNIVERSITÄT KIEL, OLSHAUSENSTRASSE 40, 24118 KIEL, GERMANY
[2]INSTITUT FÜR MINERALOGIE DER UNIVERSITÄT MÜNSTER, CORRENSSTRASSE 24, 48149 MÜNSTER, GERMANY
[3]FACULTY OF CIVIL ENGINEERING, UNIVERSITY OF ALEPPO, PO BOX 5427, ALEPPO, SYRIA

RECEIVED AUGUST 5, 2005; ACCEPTED MAY 9, 2007
ADVANCE ACCESS PUBLICATION JUNE 22, 2007

A geochemical and petrological study of Miocene to recent alkali basalts, basanites, hawaiites, mugearites, trachytes, and phonolites erupted within the Harrat Ash Shamah volcanic field was performed to reconstruct the magmatic evolution of southern Syria. The major element composition of the investigated lavas is mainly controlled by fractional crystallization of olivine, clinopyroxene, ± Fe–Ti oxides and ± apatite; feldspar fractionation is restricted to the most evolved lavas. Na_2O and SiO_2 variations within uncontaminated, primitive lavas as well as variably fractionated heavy rare earth element ratios suggest a formation by variable degrees of partial melting of different garnet peridotite sources triggered, probably, by changes in mantle temperature. The isotopic range as well as the variable trace element enrichment observed in the lavas imply derivation from both a volatile- and incompatible element-enriched asthenosphere and from a plume component. In addition, some lavas have been affected by crustal contamination. This effect is most prominent in evolved lavas older than 3·5 Ma, which assimilated 30–40% of crustal material. In general, the periodicity of volcanism in conjunction with temporal changes in lava composition and melting regime suggest that the Syrian volcanism was triggered by a pulsing mantle plume located underneath northwestern Arabia.

KEY WORDS: *$^{40}Ar/^{39}Ar$ ages; intraplate volcanism; mantle plume; partial melting; Syria*

INTRODUCTION

Continental mafic volcanic rocks exhibit large variations in chemical and isotopic compositions and their geochemical signatures can be used to constrain dynamic processes within the Earth's interior and the continental lithosphere. Magmatism in continental regions often occurs in areas of thinned lithosphere resulting in decompressional melting of the rising asthenosphere; models suggest that the volume of melt produced depends on the stretching factor of the lithosphere as well as on the temperature and composition of the asthenosphere (McKenzie & Bickle, 1988). Lithospheric thinning may be initiated either by plate boundary forces or by frictional forces exerted on the base of the lithosphere by the convecting asthenosphere (Sengör & Burke, 1978; Ziegler & Cloetingh, 2004). However, White & McKenzie (1989) suggested that lithospheric stretching without any influence of hot mantle (i.e. a mantle plume) cannot account for extensive magma generation within dry mantle peridotite. In their model continental flood basalt volcanism is restricted to the development of extreme lithospheric thinning, coinciding with the arrival of the head of a mantle plume at the base of the lithosphere and an onset of volcanism by passive upwelling of the mantle as the lithosphere thins. In contrast, Campbell & Griffiths (1990) suggested that extensive volcanism results from a starting mantle plume, but that both continental rifting and an ascending mantle plume are not necessarily required to generate large igneous provinces. Extensive melting of the mantle beneath the continents could also be due to the presence of hydrous mantle, probably in the

*Corresponding author. Present address: GeoForschungsZentrum Potsdam, Telegrafenberg, 14473 Potsdam, Germany. Telephone: +49 (0)331 288 1468. Fax: +49 (0)331 288 1474.
E-mail: krieni@gfz-potsdam.de
†Present address: Department of Earth Sciences, University of Aarhus, Høegh-Guldbergs Gade 2, 8000 Aarhus C, Denmark.

subcontinental lithosphere. The presence of hydrous phases would lower the solidus of the mantle and melting may occur in response either to lithospheric thinning at average mantle temperatures (Gallagher & Hawkesworth, 1992) or to lithospheric melting by conductive heating of the lithosphere above a mantle plume without melting the plume itself (Turner *et al.*, 1996). Thus, subcontinental lithospheric as well as asthenospheric and plume mantle sources may all contribute to magma genesis in intra-continental regions.

Rifting, faulting and volcanism in Arabia are generally linked to the two-stage evolution of the Red Sea and the Dead Sea rift systems in Miocene and Pliocene times. In addition, volcanism in southwestern Arabia has been associated with the activity of the Afar mantle plume (Schilling, 1973; Debayle *et al.*, 2001). Whereas the petrogenesis and magma source regions (i.e. crust, lithospheric mantle, asthenosphere and plume mantle) in southwestern Arabia are relatively well characterized, the causes and sources of volcanism in northern Arabia are less clear and the following models have been proposed to explain this volcanic activity: (1) lithospheric rifting mobilizing old fossil plume head material beneath the subcontinental lithosphere (Stein & Hofmann, 1992); (2) progressive lithospheric thinning tapping lithospheric (fossil plume material) to asthenospheric sources (Bertrand *et al.*, 2003; Shaw *et al.*, 2003); (3) melting of hydrous mantle lithosphere by heat conduction from sub-lithospheric anomalously hot mantle (Stein *et al.*, 1997; Weinstein *et al.*, 2006); (4) a separate mantle plume existing underneath northern Arabia (Camp & Roobol, 1992); (5) northwestward channelling of hot Afar plume material (Camp & Roobol, 1992).

This study investigates the geochemistry and isotopic signature of lavas from the largest Cenozoic intraplate volcanic field of western Arabia, the Harrat Ash Shamah in Syria, together with published data from the same volcanic field in Jordan (Shaw *et al.*, 2003) and Israel (Weinstein *et al.*, 2006) with the following objectives: (1) to determine the processes controlling the major and trace element chemistry as well as the Sr–Nd–Pb isotopic composition of the volcanic rocks; (2) to determine the geochemical characteristics of the magma sources; (3) to constrain the temporal evolution of the lavas and their mantle sources during at least 24 Myr of magmatic activity.

GEOLOGICAL SETTING

Voluminous Cenozoic alkali basaltic volcanism occurs in western Arabia, extending from Yemen over a distance of 2500 km to southeastern Turkey (Fig. 1a). These volcanic fields, the so-called Harrats, cover an area of $\sim$200 000 km^2, with an average thickness of about 100 m (Coleman *et al.*, 1983; Nasir, 1994; Tarawneh *et al.*, 2000). The Harrat Ash Shamah (or Harrat Ash-Shaam: HAS) is the largest volcanic field on the Arabian Plate and lies at the northwestern margin of the Afro-Arabian dome as outlined by Camp & Roobol (1992). The HAS strikes parallel to the Red Sea and extends some 500 km from northeastern Israel through southern Syria and Jordan to Saudi Arabia, covering more than 50 000 km^2 (Ilani *et al.*, 2001; Shaw *et al.*, 2003; Weinstein *et al.*, 2006). The volcanic field varies in width between 200 and 300 km (Tarawneh *et al.*, 2000) and the lava pile reaches a maximum thickness of 1·5 km and an altitude of $\sim$1800 m in Syria (Guba & Mustafa, 1988). The Dead Sea transform fault intersects the HAS at its northwestern edge in Israel and two small NE–SW-striking late Cretaceous graben structures lie south and north of the HAS, respectively (Almond, 1986).

The HAS mainly consists of massive lava flows, which are often separated by sedimentary horizons and red lateritic weathering crusts (Snyder *et al.*, 1993; Sharkov *et al.*, 1994); however, feeder dykes, strato- and shield volcanoes, as well as cinder cones, also occur within and on top of the lava piles. Cinder cones with a very young appearance also form the youngest eruption type. A large amount of radiometric age data are available for the HAS (Barberi *et al.*, 1980; Giannérini *et al.*, 1988; Mouty *et al.*, 1992; Mor, 1993; Sharkov *et al.*, 1994; Heimann *et al.*, 1996; Ilani *et al.*, 2001; Shaw *et al.*, 2003; Weinstein *et al.*, 2006) indicating that volcanism started about 24 Myr ago and continued to recent times with a volcanic hiatus of several million years between 13 and 7 Ma in the northern part of the HAS (Fig. 2). We present data from the northern part of the HAS field, also known as the Djebel Druze or Hauran–Druze Plateau in Syria (Ponikarov, 1969), which lies on the western flank of an uplifted region (Best *et al.*, 1990; McBride *et al.*, 1990) and can be divided into four major areas ranging in age from Miocene to historical times (Fig. 1c). The oldest flow units are of early Miocene age (24–16 Ma) and cover an area of about 200 km^2 in the northwestern part of the HAS plateau (Fig. 1c). This volcanic sequence is composed of 20–22 lava flows and is up to 400 m thick (Snyder *et al.*, 1993). These lavas unconformably overlie Cretaceous and Paleogene sediments and are covered by younger Pliocene to Quaternary lavas (Tarawneh *et al.*, 2000). Mostly Pliocene (7–3·5 Ma) volcanic rocks are concentrated in the SE, whereas the southwestern area, near the Jordan border, is covered by Pleistocene units (Fig. 1c). The youngest lavas of Holocene age form the northeastern part of the HAS. Volcanic cones up to 100 m high are the products of the youngest volcanic activity of each period and lie on the surfaces of the lava plateaux. These cones often form chains trending NW–SE and seem to trace faults that probably provided the conduits for the magmas (Giannérini *et al.*, 1988). Crustal as well as mantle xenoliths occur in several of the young volcanic cones of the HAS (Sharkov *et al.*, 1989; Nasir, 1992).

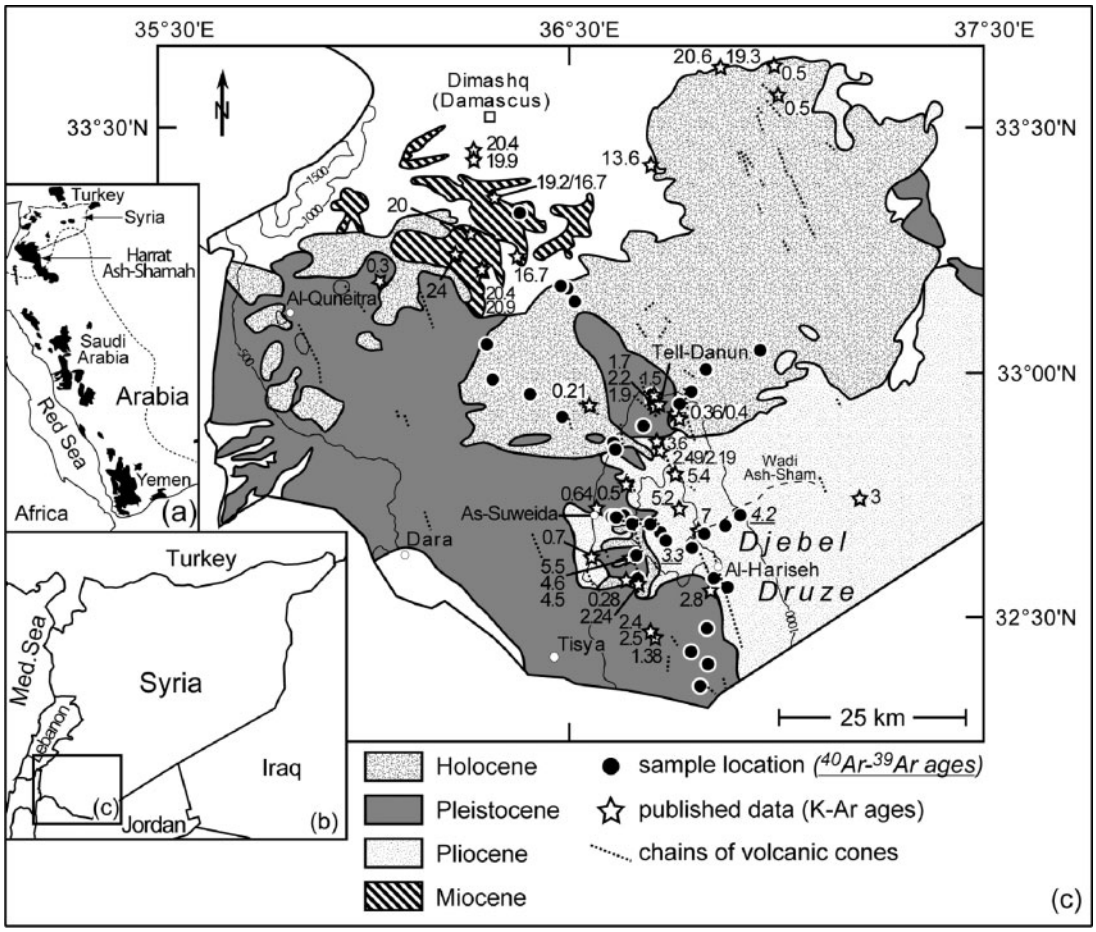

Fig. 1. (a) Distribution of volcanic fields in western Arabia. The dotted line outlines the dimensions of the Arabian part of the Afro-Arabian dome (i.e. the Arbaian swell) as suggested by Camp & Roobol (1992). (b) The study area in relation to adjacent countries. (c) Generalized geological map of the Syrian part of the Harrat Ash Shamah volcanic field showing the distribution of Miocene to Holocene volcanic rocks and sample locations. The map is based on the geological maps of Ponikarov *et al.* (1963) and on age determinations of volcanic rocks from the same rock units in Israel (Mor, 1993; Heimann *et al.*, 1996; Weinstein *et al.*, 2006). The numbers give K–Ar and $^{40}Ar/^{39}Ar$ ages in million years. Data sources: Giannérini *et al.* (1988), Mouty *et al.* (1992), Sharkov *et al.* (1994) and this study.

Precambrian crystalline basement of the Arabian–Nubian shield crops out only in southern Jordan and dips to the NE (Jarrar *et al.*, 2003). The Precambrian basement consists of gabbroic to granitic rocks that are comparable with the crustal xenoliths occurring in the lavas (Nasir, 1992, 1995). The basement in Syria is overlain by predominantly flat-lying Phanerozoic marine and continental sediments (Sharkov *et al.*, 1994). Seismic reflection data, as well as refraction profiling, have shown that the metamorphic basement lies generally deeper than 6 km (Brew *et al.*, 2001a) and varies in depth beneath the uplifted region in southern Syria between 6 km and >8 km (McBride *et al.*, 1990). Gravity and teleseismic models of the crust in southern Syria suggest a thickness of 40 ± 4 km, similar to crustal thicknesses interpreted from seismic refraction data in Jordan and Saudi Arabia (El-Isa *et al.*, 1987; Best *et al.*, 1990; McBride *et al.*, 1990; Al-Damegh *et al.*, 2005). An S receiver function study revealed a lithospheric thickness of 70–75 km in the area of the HAS (Mohsen *et al.*, 2006), which is in agreement with earlier estimates based on mantle xenoliths (McGuire & Bohannon, 1989). Seismic tomographic results show the presence of mantle material with relatively low seismic velocities at a depth of about 100 km beneath the northern part of the Arabian Plate (Debayle *et al.*, 2001).

SAMPLE PREPARATION AND ANALYTICAL METHODS

The Syrian part of the HAS volcanic field was extensively sampled and lavas from each volcanic period were collected (Fig. 1, Table 1). Hand specimens were sawn into pieces and weathered surfaces and cracks were removed.

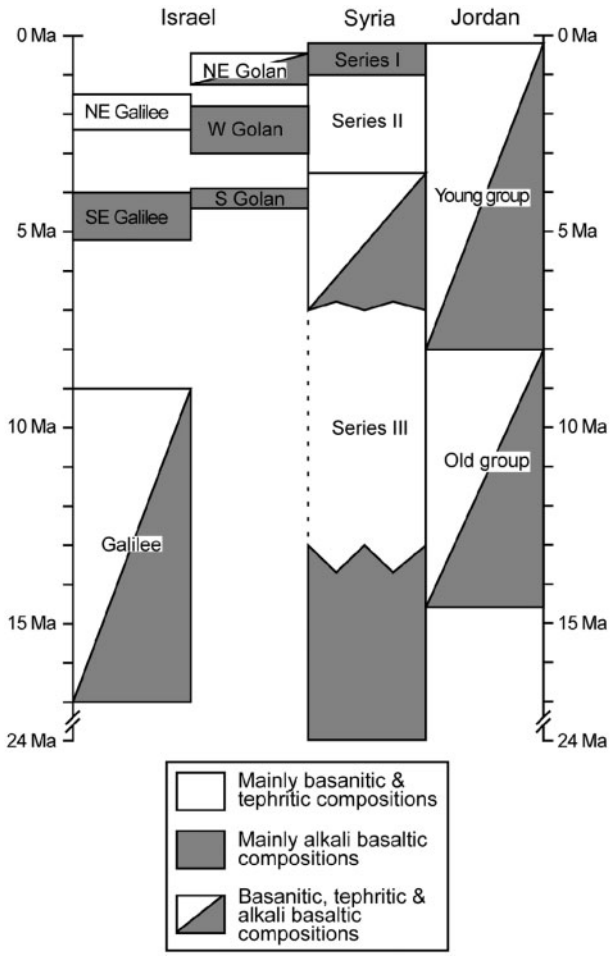

Fig. 2. Simplified stratigraphic column of the Harrat Ash Shamah volcanic field in Syria, Jordan and Israel. Data sources: Syria: this study and as in Fig. 1; Jordan: Ilani *et al.* (2001) and Shaw *et al.* (2003); Israel: Weinstein (2000) and Weinstein *et al.* (2006), and references therein.

After washing with deionized water in an ultrasonic bath the samples were crushed with a screw press and washed again. The crushed material was powdered in an agate ball mill for major and trace element and isotope analyses. Four samples contained fresh glass, which was handpicked under a binocular for chemical analysis.

The glass samples and mineral phases were analysed using a JEOL Superprobe 8900 electron microprobe at the Institut für Geowissenschaften, Universität Kiel, using standard wavelength-dispersive techniques. The instrument was operated at an accelerating voltage of 15 kV and a beam current of 15 nA. The beam diameter during calibration and measurement was set at 5 μm for glasses and feldspars and at 1 μm for the remaining phases. Counting times on peaks were set at 15 s, whereas background counting times were always set to half of peak counting times. The quality of the data was checked by repeated measurement of a set of mineral standards and the results of the glass analyses are presented in Table 2.

Major and some trace element (Cr, Ni, Zn, Rb, Sr, and Zr) analyses of whole-rock samples were performed at the Universität Kiel using a Philips PW 1400 X-ray fluorescence spectrometer, using international rock standards for calibration and data quality control. Sample powders (0·6 g) were mixed with lithium tetraborate (3·6 g) as flux and fused to glass beads. Replicate measurements of the BHVO-1 standard gave a precision better than 0·30% (SD) for all major elements and generally better than 8% (SD) for trace elements. The accuracy of standard analyses relative to reference values is generally better than 4% for most of the major and trace elements, and only Na_2O, P_2O_5 and Ni (<7%) show higher deviations (Table 2).

Trace element and rare earth element (REE) analyses were carried out by inductively coupled plasma mass spectrometry (ICP-MS) at the Universität Kiel using an upgraded PlasmaQuad PQ1 system and 100 mg of sample material. Sample preparation was performed following the method of Garbe-Schönberg (1993). Comparison of duplicate analyses of sample SY-234 gave a precision generally better than 1% (SD), except for V, Zr (<2% SD), Sr and Ba (<4% SD). The accuracy of the data based on the international rock standard BR is better than 9%, except for Cs, Nb (<10%) and Li (14%; Table 2).

Most of the Sr, Nd and Pb isotopic analyses were performed at the Zentrallaboratorium für Geochronologie in Münster using a VG Sector 54 multicollector mass spectrometer. A few Sr and Nd isotope analyses were made at the Leibniz-Institut für Meereswissenschaften in Kiel on a Finnigan Triton mass spectrometer and a few Pb isotope analyses on a Finnigan MAT 262 RPQ2+. Isotopic analyses were carried out on 100 mg of powdered sample material and standard ion exchange techniques were used to produce clean Sr, Nd and Pb separates. The samples were not leached because only fresh samples were used, which mostly also show incompatible element ratios such as Nb/U, Ce/Pb or Th/U typical of unaltered mafic rocks. Consequently, our isotope data closely resemble those of leached samples from other studies of the HAS lavas (Shaw *et al.*, 2003; Weinstein *et al.*, 2006). Isotope fractionation was corrected using $^{86}Sr/^{88}Sr = 0{\cdot}1194$ and $^{146}Nd/^{144}Nd = 0{\cdot}7219$. In Münster, standard runs for Sr isotopes gave NBS987 = 0·710299 ($n = 16$; 2SD = 0·000026) whereas in Kiel, NBS987 = 0·710252 ($n = 4$; 2SD = 0·000006). All Sr isotope analyses were normalized to NBS987 = 0·710250. Standard runs for $^{143}Nd/^{144}Nd$ in Münster yielded La Jolla = 0·511862 ($n = 14$; 2SD = 0·000024) compared with standard runs for the Nd Spex standard in Kiel, which gave values of 0·511711 ($n = 7$; 2SD = 0·000012) corresponding to a La Jolla value of 0·511855. All Nd isotope analyses were corrected to the

Table 1: Sample number, coordinates, rock type, major phenocrysts and groundmass mineralogy and sample series of the analysed Syrian volcanic rocks

Sample	Lat. (°N)	Long. (°E)	Elevation (m)	Rock type (TAS)	Phenocryst	Groundmass	Series
SY-175	33°19′37″	36°23′05″	–	alkali basalt	Ol, Cpx	Plg, Cpx, Ol	3
SY-177	33°10′47″	36°29′04″	–	alkali basalt	Ol, Cpx	Plg, Cpx, Ol	1
SY-179	33°10′16″	36°30′00″	637	alkali basalt	Ol, Plg, Cpx	Plg, Ol, Cpx	1
SY-180	33°08′54″	36°31′08″	661	alkali basalt	Ol	Plg, Mt	1
SY-184	32°42′13″	36°36′44″	1324	basanite	Ol, Cpx	Plg, Op	2
SY-186	32°42′13″	36°36′44″	1314	basanite	Ol, Cpx	Plg, Op	2
SY-189	32°42′14″	36°37′03″	1296	mugearite	Ol, Cpx	Plg, Cpx, Ol	3
SY-190	32°42′07″	36°37′13″	1306	basanite	Ol, Cpx	Plg, Cpx, Ol, Op	2
SY-191gl	32°42′07″	36°37′13″	1306	basanite	Gl	–	2
SY-192gl	32°42′07″	36°37′13″	1306	basanite	Gl	–	3
SY-193	32°42′07″	36°37′13″	1306	mugearite	–	Plg, Cpx, Op	3
SY-194	32°42′28″	36°38′31″	1450	alkali basalt	Ol, Plg, Cpx	Plg, Ol, Cpx, Op	2
SY-196	32°41′29″	36°39′43″	1603	alkali basalt	Ol, Cpx, Plg	Plg, Cpx, Ol	1
SY-197	32°41′29″	36°39′43″	1603	alkali basalt	Plg, Cpx, Ol	Plg, Cpx	1
SY-198	32°41′29″	36°39′43″	1603	alkali basalt	Plg, Cpx, Ol	Plg, Cpx	1
SY-199	32°41′20″	36°42′14″	1741	basanite	Ol, Cpx, Plg	Plg, Ol, Cpx	2
SY-200	32°41′20″	36°42′14″	1741	basanite	Cpx, Ol	Plg	2
SY-201	32°41′20″	36°42′14″	1741	basanite	Ol, Cpx	Plg	2
SY-202	32°41′25″	36°42′12″	1660	basanite	Ol, Cpx	Plg	2
SY-203	32°40′20″	36°43′59″	1763	hawaiite	Ol, Cpx	Plg, Ol, Cpx	2
SY-205	32°39′52″	36°44′35″	1797	hawaiite	Ol, Cpx, Plg	Plg, Cpx, Ol	2
SY-206	32°38′34″	36°48′19″	1555	hawaiite	Plg, Cpx, Ol	Plg, Ol, Cpx, Op	3
SY-210	32°40′04″	36°50′00″	1445	alkali basalt	Ol, Cpx	Plg, Ol, Op	3
SY-211	32°40′04″	36°50′00″	1447	alkali basalt	Cpx, Ol	Plg, Ol, Cpx, Op	3
SY-212	32°40′04″	36°50′00″	1449	alkali basalt	Ol, Cpx	Plg, Ol, Cpx, Op	3
SY-213	32°40′04″	36°50′00″	1451	alkali basalt	Ol, Cpx	Plg, Ol, Cpx, Op	3
SY-214	32°40′04″	36°50′00″	1453	alkali basalt	Ol, Cpx	Plg, Ol, Cpx, Op	3
SY-215	32°40′04″	36°50′00″	1460	alkali basalt	Ol, Plg	Plg, Ol, Cpx	3
SY-216	32°41′04″	36°53′05″	1286	basanite	Ol, Cpx	Plg, Ol, Cpx	3
SY-217	32°41′04″	36°53′05″	–	alkali basalt	Ol, Cpx, Plg	Plg, Ol, Cpx	3
SY-218	32°41′04″	36°53′05″	–	alkali basalt	Ol, Cpx, Plg	Plg, Ol, Cpx	3
SY-220	32°41′04″	36°53′05″	–	alkali basalt	Ol, Cpx, Plg	Plg, Ol, Cpx, Op	3
SY-221	32°41′04″	36°53′05″	1320	alkali basalt	Cpx, Ol, Plg	Plg, Cpx, Ol, Op	3
SY-223	32°42′40″	36°55′18″	–	hawaiite	Ol, Cpx	Plg, Ol, Cpx, Mt	3
SY-224	32°42′40″	36°55′18″	–	alkali basalt	Ol, Cpx	Plg, Cpx, Ol	3
SY-226	32°42′41″	36°55′14″	1068	alkali basalt	Ol, Plg	Plg, Cpx, Ol, Op	3
SY-227	32°42′34″	36°55′25″	1052	alkali basalt	Ol, Plg, Cpx	Plg, Cpx, Ol, Op	3
SY-228	32°34′58″	36°51′38″	1436	mugearite	Ol, Plg, Cpx	Plg, Cpx, Ol	3
SY-229	32°33′50″	36°53′39″	–	phonolite	AFsp, Cpx	AFsp, Cpx, Ol, Mt	3
SY-230	32°28′43″	36°50′36″	1374	alkali basalt	Cpx, Ol	Ol, Plg, Cpx	2
SY-234	32°25′53″	36°48′07″	–	basanite	Ol, Cpx	Plg, Ol, Cpx	2
SY-236	32°50′43″	36°37′01″	–	hawaiite	Plg, Ol, Cpx	Plg, Cpx, Ol, Op	2
SY-238	32°50′43″	36°37′01″	–	hawaiite	Plg, Ol, Cpx	Plg, Cpx, Ol, Op	2
SY-241gl	32°51′40″	36°37′00″	–	basanite	Gl		2
SY-243	32°53′46″	36°41′12″	–	basanite	Cpx, Ol	Plg, Cpx	2

(continued)

Table 1: Continued

Sample	Lat. (°N)	Long. (°E)	Elevation (m)	Rock type (TAS)	Phenocryst	Groundmass	Series
SY-245	32°57′11″	36°42′33″	1050	basanite	Cpx, Ol	Plg, Cpx, Ol	2
SY-253	32°56′02″	36°46′39″	1050	basanite	Ol, Cpx	Plg, Cpx, Ol, Op	2
SY-256	32°57′51″	36°48′09″	954	basanite	Ol	Plg, Cpx, Mt	2
SY-258	33°00′25″	36°50′20″	912	alkali basalt	Ol, Cpx	Plg, Cpx, Ol	1
SY-261	33°02′59″	36°58′16″	641	alkali basalt	Cpx, Ol	Plg, Cpx, Ol, Op	1
SY-267	32°37′41″	36°40′08″	1143	trachyte	AFsp, Ol	AFsp, Cpx, Ol, Mt	3
SY-269	32°37′41″	36°40′08″	1448	trachyte	AFsp, Ol	AFsp, Cpx	3
SY-271	32°34′53″	36°40′25″	1375	alkali basalt	Ol, Cpx, Plg	Plg, Cpx, Ol	1
SY-272	32°21′28″	36°49′38″	1260	basanite	Ol	Plg, Cpx	2
SY-273gl	32°21′28″	36°49′38″	1260	alkali basalt	Gl	Ol	2
SY-274	32°24′03″	36°50′52″	1278	basanite	Ol, Cpx	Plg, Ol, Cpx	2
SY-278	32°54′42″	36°29′25″	905	alkali basalt	Cpx, Ol	Plg, Cpx, Ol	1
SY-279	32°57′19″	36°24′53″	731	alkali basalt	Ol, Cpx	Plg, Cpx, Ol	1
SY-280	32°59′00″	36°19′07″	648	alkali basalt	Cpx, Ol	Plg, Cpx, Ol, Op	1
SY-281	33°03′30″	36°18′24″	651	alkali basalt	Cpx, Ol	Plg, Cpx, Ol, Op	1

AFsp, alkali feldspar; Cpx, clinopyroxene; Gl, glass; Mt, magnetite; Ol, olivine; Op, opaque minerals; Plg, plagioclase. Phenocryst and groundmass phases are listed in descending abundance.

La Jolla standard measured in Münster. The NBS982 standard was used to correct Pb isotopic ratios for mass fractionation in Münster. The correction factor in this laboratory is 0·1% per a.m.u. and standard runs ($n = 10$) gave $^{206}Pb/^{204}Pb = 36{\cdot}646$, $^{207}Pb/^{204}Pb = 17{\cdot}101$ and $^{208}Pb/^{204}Pb = 36{\cdot}593$ with a precision of ±0·022, ±0·014 and ±0·038 (2SD), respectively. In Kiel, repeat measurements of the NBS981 standard yielded correction factors of 0·1% per a.m.u. Standard runs ($n = 28$) yielded $^{206}Pb/^{204}Pb = 16{\cdot}903$, $^{207}Pb/^{204}Pb = 15{\cdot}447$ and $^{208}Pb/^{204}Pb = 36{\cdot}558$ with a precision of ±0·018, ±0·024 and ±0·075 (2SD), respectively. Procedural blanks during the course of the analyses were generally better than 0·2 ng, 0·1 ng and 0·04 ng for Sr, Nd and Pb, respectively (Table 3). K–Ar (Giannerini *et al.*, 1988; Mouty *et al.*, 1992; Sharkov *et al.*, 1994) and ^{40}Ar–^{39}Ar ages (this study) as well as the stratigraphic correlation indicate that the lavas chosen for isotope analyses are not older than ~4·5 Ma, and thus age corrections of the measured isotope ratios are insignificant and were not performed.

Based on thin-section investigation and on K contents two samples with unaltered groundmass were chosen and prepared for Ar–Ar dating. For analyses the crushed sample material was sieved and the 250–500 μm fraction was used to separate 50 mg of groundmass by picking under a binocular microscope. The samples were irradiated using the FRG2 reactor at the GKSS Research Centre (Geesthacht) for 7 days (Cd-liner). Irradiated samples were reloaded into aluminium trays with multiple pans holding between 4·5 and 7 mg of matrix material. The samples were heated by incrementally increasing laser power output from 0·15 to 20 W from $<350^{\circ}C$ to $>1800^{\circ}C$ until complete fusion. Software was used to control the scanning across the samples with preset patterns and a defocused laser beam, to more evenly heat the material. Automated step-heating was followed by final fusion at ~25 W with a focused beam to ensure complete degassing, and essentially evaporating the residual melt or glass sphere.

Incremental heating $^{40}Ar/^{39}Ar$ age determinations were carried out on microcrystalline groundmass separates using an Ar-ion laser combined with a MAP-216 mass spectrometer at the Leibniz-Institut für Meereswissenschaften in Kiel, Germany. Ion beam currents were measured with the electron multiplier at $m/z = 36$–40 and half-mass baselines with a 7·5 digit integrating HP multimeter. Peak heights were regressed to inlet time. The peak decay typically was less than 10% during the analyses. Average extraction line blanks are determined as 2×10^{17} mol at $m/z = 36$ and 4×10^{16} mol at $m/z = 40$. Mass discrimination was monitored using air-fused zero age basaltic glass and pipette air samples ($1{\cdot}0083 \pm 0{\cdot}0006$ a.m.u.). Correction factors for interfering neutron reactions on Ca and K were determined from co-irradiated CaF_2 and K_2SO_4 salt crystals ($^{36}Ca/^{39}Ca = 0{\cdot}445 \pm 0{\cdot}005$, $^{37}Ca/^{39}Ca = 1006 \pm 7$, $^{38}K/^{39}K = 0{\cdot}0168$, $^{40}K/^{39}K = 0{\cdot}004 \pm 0{\cdot}002$). $^{40}Ar/^{39}Ar$ ages were measured relative to the flux monitor standard TCR sanidine (27·92 Ma; Duffield & Dalrymple, 1990) and uncertainties for the J-values were estimated as

Table 2: Major (XRF) and trace element (XRF, ICP-MS) analyses of the Syrian samples, and averages of analyses of the standard BHVO-1 (XRF) and BR (ICP-MS)

Sample:	SY-175	SY-177	SY-179	SY-180	SY-184	SY-186	SY-189	SY-190	SY-191gl	SY-192gl	SY-193	SY-194	SY-196	SY-197	SY-198	SY-199	SY-200
Lat. (°N):	33°19′37″	33°10′47″	33°10′16″	33°08′54″	32°42′13″	32°42′13″	32°42′14″	32°42′07″	32°42′07″	32°42′07″	32°42′07″	32°42′28″	32°41′29″	32°41′29″	32°41′29″	32°41′20″	32°41′20″
Long. (°E):	36°23′05″	36°29′04″	36°30′00″	36°31′08″	36°36′44″	36°36′44″	36°37′03″	36°37′13″	36°37′13″	36°37′13″	36°37′13″	36°38′31″	36°39′43″	36°39′43″	36°39′43″	36°42′14″	36°42′14″
Elevation (m):	–	–	637	661	1324	1314	1296	1306	1306	1306	1306	1450	1603	1603	1603	1741	1741
Rock type:	alk. basalt	alk. basalt	alk. basalt	alk. basalt	basanite	basanite	mugearite	basanite	basanite	basanite	mugearite	alk. basalt	alk. basalt	alk. basalt	alk. basalt	basanite	basanite
SiO_2	46·15	46·03	46·26	45·37	43·63	43·92	49·28	43·00	43·44	46·16	49·39	46·75	46·01	46·47	45·88	44·17	44·95
TiO_2	2·75	2·43	2·35	2·55	3·35	3·32	2·14	3·51	3·21	3·53	2·13	2·59	2·60	2·53	2·65	2·78	2·83
Al_2O_3	14·61	14·89	14·75	15·43	15·18	15·05	17·82	14·77	14·74	17·47	17·46	16·29	16·17	16·55	16·76	15·23	15·81
Fe_2O_3T	13·13	13·61	13·69	13·08	14·30	14·08	12·50	13·62	13·69	10·37	12·22	12·69	12·58	12·52	13·05	12·77	12·93
MnO	0·13	0·17	0·17	0·16	0·17	0·18	0·17	0·17	0·18	0·15	0·18	0·17	0·17	0·17	0·17	0·18	0·18
MgO	5·90	9·07	9·69	6·98	6·78	7·22	2·60	8·40	9·06	3·84	3·24	5·80	5·62	5·80	5·95	7·69	7·69
CaO	8·43	9·06	8·95	10·37	7·89	8·02	5·68	8·79	9·02	10·40	5·89	10·41	10·17	10·25	10·08	8·46	8·53
Na_2O	3·08	3·55	3·40	3·06	4·71	4·40	4·11	4·00	3·86	5·07	5·34	3·59	3·56	3·70	2·95	4·91	4·63
K_2O	1·59	0·79	0·80	0·42	1·31	1·92	2·10	1·79	1·86	2·42	2·17	1·01	1·07	1·01	0·80	1·05	1·28
P_2O_5	0·70	0·45	0·45	0·45	0·79	0·74	1·02	0·61	0·64	0·89	1·00	0·45	0·51	0·49	0·45	0·77	0·76
LOI	3·72	0·00	0·00	1·89	1·05	0·93	1·99	0·31	0·58	–	0·28	0·00	0·00	0·00	1·20	0·36	0·51
Total	100·19	100·05	100·51	99·76	99·16	99·78	99·41	98·97	100·28	100·47	99·30	99·75	98·46	99·49	99·94	98·37	100·10
Mg-no.	0·51	0·61	0·62	0·55	0·52	0·54	0·33	0·59	0·61	0·44	0·38	0·52	0·51	0·52	0·52	0·58	0·58
Li	–	–	4·81	–	2·97	–	–	–	–	7·62	–	3·59	–	–	–	–	2·03
Sc	–	–	15·6	–	10·1	–	–	–	–	18·7	–	25·5	–	–	–	–	14·7
V	–	–	–	–	122	–	–	–	–	–	–	255	–	–	–	–	134
Cr	167	253	253	172	68·9	107	–	130	155	131	–	106	106	101	100	134	93·3
Co	–	–	55·4	–	38·4	–	–	–	–	54·8	–	44·1	–	–	–	–	35·0
Ni	169	199	209	61	78·7	118	9	161	170	170	2	44·7	42	46	52	139	92·6
Cu	–	–	59·0	–	29·1	–	–	–	–	55·4	–	67·5	–	–	–	–	30·8
Zn	146	113	112	100	106	122	97	97	103	110	95	105	97	103	106	89	77·4
Ga	–	–	21·3	–	33·4	–	–	–	–	–	–	24·3	–	–	–	–	29·0
Rb	18	9	9·79	3	22·3	32	22	34	31	38·9	31	12·5	15	15	8	36	39·5
Y	–	–	21·0	–	22·3	–	–	–	–	22·0	–	24·9	–	–	–	–	25·4
Cs	–	–	0·079	–	0·469	–	–	–	–	0·385	–	0·079	–	–	–	–	0·354
Sr	258	539	530	560	1016	977	945	802	861	812	943	641	586	613	638	833	883
Ba	–	–	198	–	401	–	–	–	–	396	–	263	–	–	–	–	375

(continued)

Table 2: Continued

Sample:	SY-175	SY-177	SY-179	SY-180	SY-184	SY-186	SY-189	SY-190	SY-191gl	SY-192gl	SY-193	SY-194	SY-196	SY-197	SY-198	SY-199	SY-200
Lat. (°N):	33°19′37″	33°10′47″	33°10′16″	33°08′54″	32°42′13″	32°42′13″	32°42′14″	32°42′07″	32°42′07″	32°42′07″	32°42′07″	32°42′28″	32°41′29″	32°41′29″	32°41′29″	32°41′20″	32°41′20″
Long. (°E):	36°23′05″	36°29′04″	36°30′00″	36°31′08″	36°36′44″	36°36′44″	36°37′03″	36°37′13″	36°37′13″	36°37′13″	36°37′13″	36°38′31″	36°39′43″	36°39′43″	36°39′43″	36°42′14″	36°42′14″
Elevation (m):	–	–	637	661	1324	1314	1296	1306	1306	1306	1306	1450	1603	1603	1603	1741	1741
Rock type:	alk. basalt	alk. basalt	alk. basalt	alk. basalt	basanite	basanite	mugearite	basanite	basanite	basanite	mugearite	alk. basalt	alk. basalt	alk. basalt	alk. basalt	basanite	basanite
Zr	444	186	152	192	312	359	355	269	387	248	3	172	195	185	196	329	289
Hf	–	–	3·70	–	8·16	–	–	–	–	5·89	–	3·43	–	–	–	–	7·48
Nb	–	–	24·1	–	48·0	–	–	–	–	50·8	–	30·6	–	–	–	–	53·0
Ta	–	–	1·47	–	3·11	–	–	–	–	1·58	–	1·64	–	–	–	–	3·77
Pb	–	–	1·55	–	2·85	–	–	–	–	2·82	–	1·77	–	–	–	–	2·70
Th	–	–	1·83	–	4·13	–	–	–	–	4·41	–	1·66	–	–	–	–	4·02
U	–	–	0·413	–	1·15	–	–	–	–	1·27	–	0·464	–	–	–	–	1·23
La	–	–	20·2	–	41·8	–	–	–	–	36·2	–	20·1	–	–	–	–	40·1
Ce	–	–	44·0	–	88·1	–	–	–	–	73·9	–	44·5	–	–	–	–	83·2
Pr	–	–	5·54	–	11·2	–	–	–	–	8·83	–	5·53	–	–	–	–	10·3
Nd	–	–	23·7	–	45·5	–	–	–	–	35·4	–	23·6	–	–	–	–	40·8
Sm	–	–	5·40	–	9·52	–	–	–	–	7·35	–	5·53	–	–	–	–	8·49
Eu	–	–	1·85	–	3·06	–	–	–	–	2·35	–	2·01	–	–	–	–	2·75
Gd	–	–	5·28	–	8·40	–	–	–	–	6·85	–	5·27	–	–	–	–	7·63
Tb	–	–	0·755	–	1·193	–	–	–	–	0·938	–	0·777	–	–	–	–	1·142
Dy	–	–	4·19	–	5·99	–	–	–	–	4·92	–	4·29	–	–	–	–	6·18
Ho	–	–	0·763	–	0·995	–	–	–	–	0·861	–	0·807	–	–	–	–	1·12
Er	–	–	1·90	–	2·38	–	–	–	–	2·11	–	2·10	–	–	–	–	2·87
Tm	–	–	0·248	–	0·290	–	–	–	–	0·276	–	0·313	–	–	–	–	0·387
Yb	–	–	1·53	–	1·74	–	–	–	–	1·66	–	1·82	–	–	–	–	2·39
Lu	–	–	0·210	–	0·244	–	–	–	–	0·235	–	0·242	–	–	–	–	0·345

(continued)

Table 2: Continued

Sample:	SY-201	SY-202	SY-203	SY-205	SY-206	SY-210	SY-211	SY-212	SY-213	SY-214	SY-215	SY-216	SY-217	SY-218	SY-220	SY-221	SY-223
Lat. (°N):	32°41′20″	32°41′25″	32°40′20″	32°39′52″	32°38′34″	32°40′04″	32°40′04″	32°40′04″	32°40′04″	32°40′04″	32°40′04″	32°41′04″	32°41′04″	32°41′04″	32°41′04″	32°41′04″	32°42′40″
Long. (°E):	36°42′14″	36°42′12″	36°43′59″	36°44′35″	36°48′19″	36°50′00″	36°50′00″	36°50′00″	36°50′00″	36°50′00″	36°50′00″	36°53′05″	36°53′05″	36°53′05″	36°53′05″	36°53′05″	36°55′18″
Elevation (m):	1741	1660	1763	1797	1555	1445	1447	1449	1451	1453	1460	1286	–	–	–	1320	–
Rock type:	basanite	basanite	hawaiite	hawaiite	hawaiite	alk. basalt	alk. basalt	alk. basalt	alk. basalt	alk. basalt	alk. basalt	basanite	alk. basalt	alk. basalt	alk. basalt	alk. basalt	hawaiite
SiO_2	44·77	44·30	45·12	45·10	46·96	46·10	46·16	46·48	45·99	46·25	46·27	42·74	46·95	46·94	46·90	46·95	44·26
TiO_2	2·84	2·85	3·04	3·13	2·83	2·25	2·23	2·20	2·17	2·13	2·35	3·36	1·99	2·01	2·01	2·02	3·11
Al_2O_3	15·64	15·31	14·75	15·16	17·31	15·45	15·48	15·75	15·58	15·45	15·56	16·15	14·91	15·08	14·92	15·00	14·34
Fe_2O_3T	13·00	12·83	12·06	12·09	11·91	13·25	12·96	13·02	12·76	12·52	12·41	14·28	12·12	12·04	12·10	12·05	12·31
MnO	0·18	0·18	0·16	0·16	0·16	0·16	0·17	0·17	0·16	0·15	0·16	0·20	0·16	0·16	0·17	0·17	0·16
MgO	7·51	7·47	6·56	5·82	4·12	7·63	7·69	7·40	7·35	7·55	7·48	4·97	9·15	8·62	9·03	8·74	7·91
CaO	8·43	8·39	10·27	10·10	9·10	9·48	9·79	9·73	9·64	10·03	10·62	8·68	9·36	9·55	9·61	9·62	10·17
Na_2O	3·50	4·49	3·77	3·65	4·23	2·72	3·11	3·08	2·64	2·69	3·18	3·65	3·02	3·07	3·15	3·18	3·20
K_2O	2·04	0·86	1·46	1·51	1·50	0·76	0·73	0·76	0·80	0·78	0·82	1·42	0·97	1·02	0·98	0·99	1·67
P_2O_5	0·77	0·75	1·10	1·19	0·53	0·38	0·37	0·39	0·39	0·37	0·44	1·30	0·30	0·31	0·30	0·31	1·03
LOI	0·10	0·77	0·68	0·52	0·39	1·18	0·25	0·86	0·92	1·17	0·17	1·61	0·00	0·11	0·02	0·06	1·42
Total	98·78	98·20	98·97	98·43	99·04	99·36	98·94	99·84	98·40	99·09	99·46	98·36	98·93	98·91	99·19	99·09	99·58
Mg-no.	0·57	0·58	0·56	0·53	0·45	0·57	0·58	0·57	0·57	0·58	0·58	0·45	0·64	0·63	0·63	0·63	0·60
Li	–	2·23	–	5·04	8·95	3·82	–	5·21	5·37	–	4·07	8·72	–	–	–	7·67	–
Sc	–	14·6	–	18·1	14·3	23·1	–	18·4	18·9	–	24·7	11·6	–	–	–	20·6	–
V	–	130	–	–	–	237	–	–	–	–	248	–	–	–	–	–	–
Cr	143	83·7	157	119	39·0	281	279	285	263	274	227	18·0	364	335	363	332	192
Co	–	34·4	–	42·1	31·9	47·0	–	45·8	46·6	–	51·2	37·0	–	–	–	49·4	–
Ni	126	79·3	83	61·0	34·0	120	126	129	116	107	95·5	17·0	195	173	181	168	131
Cu	–	26·3	–	49·2	33·0	52·0	–	52·5	53·8	–	54·5	27·2	–	–	–	59·4	–
Zn	86	76·7	116	111	103	100	104	99·0	106	97	99·3	104	96	95	93	92·0	118
Ga	–	28·4	–	26·6	25·4	21·3	–	20·8	21·6	–	22·3	22·3	–	–	–	21·4	–
Rb	28	27·2	20	17·6	25·0	8·41	6	9·30	10·1	11	10·8	19·6	21	25	23	21·6	27
Y	–	25·3	–	25·7	26·7	19·2	–	19·8	20·8	–	20·1	29·7	–	–	–	23·9	–
Cs	–	0·343	–	0·148	0·418	0·046	–	0·072	0·072	–	0·106	0·454	–	–	–	0·358	–
Sr	884	858	1634	1711	733	530	577	576	582	587	665	1411	478	493	486	494	1519
Ba	–	362	–	662	276	217	–	209	233	–	240	–	–	–	–	197	–
Zr	339	287	330	257	216	130	161	126	134	164	160	324	168	170	168	147	364

(continued)

Table 2: Continued

Sample:	SY-201	SY-202	SY-203	SY-205	SY-206	SY-210	SY-211	SY-212	SY-213	SY-214	SY-215	SY-216	SY-217	SY-218	SY-220	SY-221	SY-223
Lat. (°N):	32°41′20″	32°41′25″	32°40′20″	32°39′52″	32°38′34″	32°40′04″	32°40′04″	32°40′04″	32°40′04″	32°40′04″	32°40′04″	32°41′04″	32°41′04″	32°41′04″	32°41′04″	32°41′04″	32°42′40″
Long. (°E):	36°42′14″	36°42′12″	36°43′59″	36°44′35″	36°48′19″	36°50′00″	36°50′00″	36°50′00″	36°50′00″	36°50′00″	36°50′00″	36°53′05″	36°53′05″	36°53′05″	36°53′05″	36°53′05″	36°55′18″
Elevation (m):	1741	1660	1763	1797	1555	1445	1447	1449	1451	1453	1460	1286	–	–	–	1320	–
Rock type:	basanite	basanite	hawaiite	hawaiite	hawaiite	alk. basalt	alk. basalt	alk. basalt	alk. basalt	alk. basalt	alk. basalt	basanite	alk. basalt	alk. basalt	alk. basalt	alk. basalt	hawaiite
Hf	–	7·30	–	5·82	5·14	3·16	–	3·17	3·47	–	3·40	6·32	–	–	–	3·82	–
Nb	–	51·4	–	52·8	41·9	23·6	–	22·5	24·3	–	30·3	89·3	–	–	–	23·3	–
Ta	–	3·62	–	3·06	2·73	1·46	–	1·35	1·45	–	1·66	4·96	–	–	–	1·58	–
Pb	–	3·02	–	2·79	2·79	1·62	–	6·43	1·62	–	1·68	3·08	–	–	–	2·55	–
Th	–	4·01	–	2·91	3·31	1·89	–	1·84	2·04	–	2·06	4·74	–	–	–	2·46	–
U	–	1·24	–	0·882	1·13	0·531	–	0·497	0·529	–	0·555	1·32	–	–	–	0·831	–
La	–	38·9	–	51·2	27·8	18·9	–	18·4	20·0	–	21·7	58·5	–	–	–	17·3	–
Ce	–	80·9	–	107	58·7	39·6	–	38·5	41·7	–	46·4	118	–	–	–	38·1	–
Pr	–	10·0	–	13·2	7·25	4·92	–	4·74	5·12	–	5·52	13·8	–	–	–	4·85	–
Nd	–	40·0	–	54·1	29·8	20·4	–	20·0	21·6	–	22·7	53·7	–	–	–	20·3	–
Sm	–	8·29	–	10·6	6·57	4·68	–	4·63	4·91	–	5·03	10·0	–	–	–	4·95	–
Eu	–	2·67	–	3·54	2·13	1·67	–	1·61	1·68	–	1·84	3·16	–	–	–	1·54	–
Gd	–	7·47	–	8·86	6·36	4·67	–	4·57	4·85	–	4·86	8·66	–	–	–	4·97	–
Tb	–	1·120	–	1·117	0·926	0·695	–	0·688	0·717	–	0·696	1·137	–	–	–	0·762	–
Dy	–	6·11	–	5·61	5·26	3·94	–	3·87	4·06	–	3·81	6·02	–	–	–	4·52	–
Ho	–	1·11	–	0·948	0·976	0·734	–	0·716	0·753	–	0·707	1·07	–	–	–	0·843	–
Er	–	2·85	–	2·25	2·51	1·87	–	1·83	1·92	–	1·80	2·68	–	–	–	2·24	–
Tm	–	0·379	–	0·280	0·341	0·249	–	0·244	0·254	–	0·254	0·351	–	–	–	0·307	–
Yb	–	2·41	–	1·67	2·14	1·52	–	1·48	1·54	–	1·54	2·14	–	–	–	1·97	–
Lu	–	0·342	–	0·225	0·298	0·213	–	0·207	0·223	–	0·209	0·303	–	–	–	0·276	–

(continued)

Table 2: Continued

Sample:	SY-224	SY-226	SY-227	SY-228	SY-229	SY-230	SY-236	SY-238	SY-241gl	SY-243	SY-245	SY-253	SY-256	SY-258	SY-261	SY-267	SY-269
Lat. (°N):	32°42′40″	32°42′41″	32°42′34″	32°34′58″	32°33′50″	32°28′43″	32°50′43″	32°50′43″	32°51′40″	32°53′46″	32°57′11″	32°56′02″	32°57′51″	33°00′25″	33°02′59″	32°37′41″	32°37′41″
Long. (°E):	36°55′18″	36°55′14″	36°55′25″	36°51′38″	36°53′39″	36°50′36″	36°37′01″	36°37′01″	36°37′00″	36°41′12″	36°42′33″	36°46′39″	36°48′09″	36°50′20″	36°58′16″	36°40′08″	36°40′08″
Elevation (m):	–	1068	1052	1436	–	1374	–	–	–	–	1050	1050	954	912	641	1143	1448
Rock type:	alk. basalt	alk. basalt	alk. basalt	mugearite	phonolite	alk. basalt	hawaiite	hawaiite	basanite	basanite	basanite	basanite	basanite	alk. basalt	alk. basalt	trachyte	trachyte
SiO_2	43·51	46·40	47·12	49·36	55·80	47·89	46·46	46·17	46·17	45·49	43·52	42·12	43·66	45·35	46·43	60·22	59·48
TiO_2	2·99	2·55	2·07	2·37	0·41	2·04	3·21	3·18	3·25	2·45	2·87	2·73	3·18	2·05	2·04	0·30	0·29
Al_2O_3	14·17	15·90	14·86	17·05	19·33	16·34	16·42	16·31	17·16	14·71	15·13	13·74	14·47	14·40	15·95	18·02	17·70
Fe_2O_3T	12·20	12·45	12·11	11·08	6·64	11·75	12·15	12·09	11·18	12·78	12·67	12·78	13·37	12·48	12·20	5·24	5·43
MnO	0·16	0·17	0·16	0·18	0·12	0·16	0·16	0·16	0·18	0·17	0·17	0·18	0·18	0·16	0·17	0·14	0·18
MgO	8·15	6·12	8·75	2·92	0·88	6·61	5·05	4·98	3·76	8·66	7·27	9·82	8·10	8·99	7·22	0·23	0·25
CaO	10·40	10·97	9·59	7·18	2·05	9·69	9·67	9·60	9·20	7·99	9·59	10·46	8·62	10·42	10·05	1·54	1·64
Na_2O	2·80	3·86	3·13	5·16	8·84	3·24	4·31	4·44	5·24	4·70	4·87	3·86	4·45	3·08	3·15	7·37	7·17
K_2O	1·81	0·69	1·02	2·18	3·44	0·84	1·52	1·54	2·24	1·72	0·93	0·73	1·45	0·75	0·72	4·93	4·84
P_2O_5	0·99	0·41	0·31	0·90	0·35	0·33	0·67	0·68	1·02	0·70	0·90	0·74	0·84	0·32	0·37	0·12	0·14
LOI	1·85	0·09	0·03	0·58	1·38	0·14	0·14	0·35	–	0·00	1·43	1·73	1·81	0·69	2·68	0·41	0·74
Total	99·03	99·61	99·15	98·96	99·24	99·03	99·76	99·50	99·60	99·37	99·35	98·89	100·13	98·69	100·98	98·52	102·69
Mg-no.	0·61	0·53	0·63	0·38	0·24	0·57	0·49	0·49	0·41	0·61	0·57	0·64	0·59	0·63	0·58	0·09	0·10
Li	6·92	1·93	8·51	–	–	–	4·58	–	8·80	–	–	–	–	1·72	5·01	24·6	19·9
Sc	16·8	18·1	20·6	–	–	–	21·8	–	17·5	–	–	–	–	16·4	20·4	2·32	2·32
V	–	163	–	–	–	–	255	–	–	–	–	–	–	139	–	–	–
Cr	209	101	323	1	n.d.	170	55·2	55	107	245	185	267	205	254	185	> 1	> 1
Co	43·9	33·2	47·8	–	–	–	40·3	–	55·6	–	–	–	–	42·4	45·2	1·26	1·22
Ni	143	36·5	175	n.d.	n.d.	74	31·6	26	148	205	117	200	163	145	86·0	> 1	> 1
Cu	51·6	41·6	62·7	–	–	–	54·4	–	47·1	–	–	–	–	36·9	55·5	8·27	8·74
Zn	115	87·5	93·0	114	154	98	117	105	118	105	99	103	115	81·0	98·0	110	110
Ga	22·7	28·5	21·1	–	–	–	26·0	–	–	–	–	–	–	30·3	22·1	–	–
Rb	19·6	6·95	22·4	39	42	9	20·8	26	38·9	24	8	7	16	10·6	8·42	59·7	52·5
Y	23·2	20·6	24·2	–	–	–	25·1	–	23·9	–	–	–	–	17·2	24·3	32·4	32·5
Cs	0·178	0·080	0·443	–	–	–	0·174	–	0·375	–	–	–	–	0·059	0·066	0·877	0·637
Sr	1536	517	483	698	846	496	902	815	850	798	963	917	1133	561	463	109	240
Ba	588	333	189	–	–	–	386	–	391	–	–	–		473	204	765	757
Zr	272	142	150	328	574	160	251	270	279	308	320	300	378	122	159	848	866

(continued)

Table 2: Continued

Sample:	SY-224	SY-226	SY-227	SY-228	SY-229	SY-230	SY-236	SY-238	SY-241gl	SY-243	SY-245	SY-253	SY-256	SY-258	SY-261	SY-267	SY-269
Lat. (°N):	32°42′40″	32°42′41″	32°42′34″	32°34′58″	32°33′50″	32°28′43″	32°50′43″	32°50′43″	32°51′40″	32°53′46″	32°57′11″	32°56′02″	32°57′51″	33°00′25″	33°02′59″	32°37′41″	32°37′41″
Long. (°E):	36°55′18″	36°55′14″	36°55′25″	36°51′38″	36°53′39″	36°50′36″	36°37′01″	36°37′01″	36°37′00″	36°41′12″	36°42′33″	36°46′39″	36°48′09″	36°50′20″	36°58′16″	36°40′08″	36°40′08″
Elevation (m):	–	1068	1052	1436	–	1374	–	–	–	–	1050	1050	954	912	641	1143	1448
Rock type:	alk. basalt	alk. basalt	alk. basalt	mugearite	phonolite	alk. basalt	hawaiite	hawaiite	basanite	basanite	basanite	basanite	basanite	alk. basalt	alk. basalt	trachyte	trachyte
Hf	5·83	4·08	3·70	–	–	–	4·69	–	6·44	–	–	–	–	3·60	3·86	19·5	19·8
Nb	55·6	19·3	23·9	–	–	–	52·5	–	46·7	–	–	–	–	20·2	22·0	93·3	94·0
Ta	3·32	1·34	1·61	–	–	–	2·77	–	2·43	–	–	–	–	1·37	1·35	7·09	7·13
Pb	3·07	1·40	2·41	–	–	–	2·48	–	2·52	–	–	–	–	1·52	1·54	11·8	11·6
Th	3·49	1·30	2·50	–	–	–	2·56	–	4·00	–	–	–	–	1·40	1·33	13·0	13·3
U	0·806	0·341	0·891	–	–	–	0·669	–	1·18	–	–	–	–	0·381	0·301	3·58	2·72
La	49·9	16·4	17·7	–	–	–	31·9	–	37·7	–	–	–	–	17·7	18·3	69·5	67·8
Ce	102	38·2	38·3	–	–	–	68·8	–	79·2	–	–	–	–	38·6	40·6	129	126
Pr	12·2	5·27	4·85	–	–	–	8·29	–	9·59	–	–	–	–	5·06	5·16	13·7	13·4
Nd	49·4	23·2	20·6	–	–	–	34·1	–	38·2	–	–	–	–	21·5	22·1	46·1	45·3
Sm	9·47	5·76	4·93	–	–	–	7·30	–	7·93	–	–	–	–	5·02	5·07	7·96	7·90
Eu	3·06	2·03	1·57	–	–	–	2·72	–	2·53	–	–	–	–	1·78	1·72	1·69	1·65
Gd	7·99	5·75	4·98	–	–	–	6·54	–	7·33	–	–	–	–	4·90	5·13	7·28	7·26
Tb	1·010	0·883	0·766	–	–	–	0·890	–	0·998	–	–	–	–	0·753	0·775	1·107	1·097
Dy	5·12	5·03	4·49	–	–	–	4·60	–	5·26	–	–	–	–	4·24	4·60	6·68	6·61
Ho	0·863	0·932	0·857	–	–	–	0·816	–	0·935	–	–	–	–	0·782	0·891	1·36	1·36
Er	2·07	2·35	2·27	–	–	–	2·04	–	2·34	–	–	–	–	1·96	2·34	3·99	4·01
Tm	0·260	0·311	0·312	–	–	–	0·291	–	0·302	–	–	–	–	0·262	0·321	0·630	0·628
Yb	1·53	1·93	1·95	–	–	–	1·71	–	1·83	–	–	–	–	1·61	2·01	4·46	4·49
Lu	0·209	0·275	0·278	–	–	–	0·222	–	0·263	–	–	–	–	0·232	0·289	0·703	0·701

(continued)

Table 2: Continued

Sample:	SY-271	SY-272	SY-273gl	SY-274	SY-278	SY-279	SY-280	SY-281	SY-234(1)	SY-234(2)	SY-234(mean)	BHVO-1 (XRF)	BR (ICP-MS)
Lat. (°N):	32°34′53″	32°21′28″	32°21′28″	32°24′03″	32°54′42″	32°57′19″	32°59′00″	33°03′30″			32°25′53″		
Long. (°E):	36°40′25″	36°49′38″	36°49′38″	36°50′52″	36°29′25″	36°24′53″	36°19′07″	36°18′24″			36°48′07″		
Elevation (m):	1375	1260	1260	1278	905	731	648	651			–	standard	standard
Rock type:	alk. basalt	basanite	alk. basalt	basanite	alk. basalt	alk. basalt	alk. basalt	alk. basalt			basanite	($n=9$)	($n=3$)
SiO_2	47·60	42·53	46·57	43·29	47·08	47·02	44·99	45·92			44·55	49·68	–
TiO_2	2·47	2·56	3·26	3·24	2·26	2·31	2·45	2·60			2·33	2·74	–
Al_2O_3	16·35	13·05	16·95	14·98	15·86	16·16	14·09	14·51			14·76	13·72	–
Fe_2O_3T	12·09	13·19	11·58	13·11	12·20	12·21	13·66	13·76			13·88	12·03	–
MnO	0·16	0·18	0·14	0·17	0·16	0·16	0·17	0·18			0·21	0·17	–
MgO	6·19	11·40	5·06	8·70	6·43	6·37	9·26	9·39			6·73	7·26	–
CaO	9·34	9·17	10·77	8·95	9·77	9·94	9·41	9·44			8·06	11·34	–
Na_2O	3·62	3·64	2·57	4·14	3·33	3·49	3·28	3·13			4·86	2·37	–
K_2O	1·10	0·65	2·29	1·99	1·00	0·88	0·87	0·83			2·10	0·53	–
P_2O_5	0·42	0·77	0·99	0·67	0·45	0·39	0·48	0·48			0·91	0·28	–
LOI	0·26	1·84	–	0·03	0·03	0·00	0·00	0·00			0·83	–	–
Total	99·60	98·98	100·33	99·27	98·57	98·93	98·66	100·24			99·22	100·13	–
Mg-no.	0·54	0·67	0·48	0·61	0·55	0·55	0·61	0·61			0·53		
Li	–	–	1·91	–	1·95	1·96	1·63	–	3·16	3·27	3·22	–	11·4
Sc	–	–	24·3	–	15·7	16·1	14·8	–	11·7	12·2	12·0	–	19·9
V	–	–	–	–	148	145	138	–	145	152	149	–	217
Cr	113	363	307	164	109	119	189	246	122	126	124	286	353
Co	–	–	52·9	–	33·7	33·5	44·5	–	43·5	43·7	43·6	–	54·6
Ni	67	387	183	161	53·7	53·9	154	210	126	127	126	108	249
Cu	–	–	5·41	–	38·0	38·5	48·0	–	38·1	38·5	38·3	–	65·9
Zn	97	97	99·1	93	84·8	85·4	93·7	119	123	126	125	102	149
Ga	–	–	–	–	25·3	25·7	24·5	–	24·2	24·4	24·3	–	18·1
Rb	17	7	29·6	22	16·0	11·4	11·4	15	26·1	27·1	26·6	11	27·4
Y	–	–	22·7	–	22·0	22·1	20·6	–	26·0	26·7	26·3	–	45·6
Cs	–	–	0·431	–	0·188	0·106	0·106	–	0·464	0·490	0·477	–	0·743
Sr	692	944	739	881	545	563	559	549	1282	1293	1288	396	1365
Ba	–	–	351	–	232	232	235	–	452	466	459	–	1058
Zr	205	281	234	302	187	185	165	192	381	388	384	184	267

(continued)

Table 2: Continued

Sample:	SY-271	SY-272	SY-273gl	SY-274	SY-278	SY-279	SY-280	SY-281	SY-234(1)	SY-234(2)	SY-234(mean)	BHVO-1 (XRF)	BR (ICP-MS)
Lat. (°N):	32°34′53″	32°21′28″	32°21′28″	32°24′03″	32°54′42″	32°57′19″	32°59′00″	33°03′30″			32°25′53″		
Long. (°E):	36°40′25″	36°49′38″	36°49′38″	36°50′52″	36°29′25″	36°24′53″	36°19′07″	36°18′24″			36°48′07″		
Elevation (m):	1375	1260	1260	1278	905	731	648	651			–	standard	standard
Rock type:	alk. basalt	basanite	alk. basalt	basanite	alk. basalt	alk. basalt	alk. basalt	alk. basalt			basanite	($n=9$)	($n=3$)
Hf	–	–	5·60	–	5·25	5·15	4·69	–	6·52	6·81	6·67	–	5·90
Nb	–	–	46·1	–	27·0	27·0	26·4	–	69·1	71·2	70·2	–	105
Ta	–	–	2·91	–	1·82	1·82	1·77	–	3·84	3·96	3·90	–	5·58
Pb	–	–	2·46	–	1·98	1·91	1·93	–	4·67	4·74	4·70	–	4·42
Th	–	–	3·73	–	2·13	2·01	2·24	–	5·92	6·09	6·01	–	10·6
U	–	–	1·19	–	1·23	0·557	0·615	–	1·71	1·72	1·72	–	2·48
La	–	–	36·1	–	26·6	25·7	24·5	–	60·0	61·6	60·8	–	79·8
Ce	–	–	75·0	–	56·9	55·2	53·6	–	120	123	121	–	151
Pr	–	–	9·00	–	7·30	7·14	7·04	–	13·1	13·5	13·3	–	16·8
Nd	–	–	36·3	–	30·2	29·9	29·8	–	49·1	50·1	49·6	–	64·3
Sm	–	–	7·50	–	6·71	6·70	6·82	–	9·43	9·50	9·47	–	12·0
Eu	–	–	2·35	–	2·19	2·25	2·31	–	3·26	3·29	3·28	–	3·55
Gd	–	–	6·99	–	6·35	6·41	6·44	–	7·95	8·08	8·02	–	9·94
Tb	–	–	0·961	–	0·972	0·973	0·955	–	1·06	1·09	1·074	–	1·29
Dy	–	–	5·10	–	5·41	5·40	5·14	–	5·10	5·28	5·19	–	6·37
Ho	–	–	0·911	–	0·995	0·987	0·927	–	0·855	0·868	0·862	–	1·07
Er	–	–	2·27	–	2·52	2·51	2·28	–	2·02	2·02	2·02	–	2·53
Tm	–	–	0·295	–	0·337	0·337	0·301	–	0·265	0·265	0·265	–	0·307
Yb	–	–	1·82	–	2·12	2·10	1·83	–	1·44	1·46	1·45	–	1·80
Lu	–	–	0·254	–	0·301	0·303	0·262	–	0·175	0·180	0·177	–	0·241

Table 3: Sr, Nd, and Pb isotopic compositions of selected Syrian lavas

Sample	$^{87}Sr/^{86}Sr$ (2σ)	$^{143}Nd/^{144}Nd$ (2σ)	$^{206}Pb/^{204}Pb$	$^{207}Pb/^{204}Pb$	$^{208}Pb/^{204}Pb$
SY-179	0·703314 (9)	0·512837 (13)	19·122	15·634	39·020
SY-184	0·703259 (2)	0·512934 (2)	19·194	15·574	38·891
SY-200	0·703094 (3)	0·512940 (2)			
SY-202	0·703048 (3)	0·512944 (2)	19·115	15·568	38·768
SY-213	0·703413 (11)	0·512910 (12)	19·102	15·622	38·996
SY-216	0·703298 (13)	0·512913 (12)	19·107	15·627	38·938
SY-221	0·703859 (14)	0·512887 (10)	19·443	15·649	38·829
SY-224	0·703425 (10)	0·512895 (10)	19·046	15·615	38·839
SY-227	0·703962 (11)	0·512861 (14)	19·276	15·646	38·729
SY-234	0·703118 (10)	0·512989 (7)	19·046	15·586	38·778
SY-261	0·703318 (9)	0·512840 (12)	18·854	15·613	38·687
SY-279	0·703313 (3)		18·998	15·602	38·779
SY-280	0·703301 (3)	0·512843 (3)	19·055	15·598	38·840

±0·08% (1σ). Incremental heating plateau ages were calculated as weighted mean (Taylor, 1982) and initial $^{40}Ar/^{36}Ar$ isotope ratios and isochron ages as least-squares fits with correlated errors (York, 1969) applying the decay constants of Steiger & Jäger (1977). The results are compiled in Table 4.

PETROGRAPHIC AND GEOCHEMICAL CHARACTERISTICS

Petrography

Hand specimens of the investigated volcanic rocks are generally fresh, with only a few samples showing evidence of alteration. Almost all samples have porphyritic textures and contain variable amounts of phenocrysts, with olivine and clinopyroxene being the most abundant and feldspars rare. Most olivines show iddingsite rims and some are completely altered. The predominant feldspar is plagioclase but in the trachytic and phonolitic lavas mainly alkali feldspars occur (Table 1). The mostly fine-grained groundmass consists of olivine, clinopyroxene, plagioclase, and Fe–Ti oxides. Rare calcite-filled vesicles are visible in hand specimen. Some lava samples contain agglomerates of clinopyroxene and olivine phenocrysts. Sample SY-272 contains a mantle xenolith ~8 mm in diameter, composed of mainly olivine and orthopyroxene with strongly resorbed rims, which is classified as wehrlite.

Classification

In the total alkali vs silica diagram the HAS samples are mainly of basaltic and basanitic–tephritic composition, whereas evolved lavas are rare (Fig. 3). All basaltic rocks fall into the alkaline field using the division line of MacDonald (1968) and, except for four samples, all basalts are nepheline-normative and thus can be classified as alkali basalts. The lavas from the northeastern Syrian part of the HAS resemble those found in the south (Jordan, Shaw *et al.*, 2003) and western edge (Israel, Weinstein *et al.*, 2006) of the HAS (Fig. 3). To study the chemical evolution of the HAS magmatism we grouped the entire dataset into three series based on their relative stratigraphic age, on published K–Ar ages (Giannérini *et al.*, 1988; Mouty *et al.*, 1992; Sharkov *et al.*, 1994) and on ^{40}Ar–^{39}Ar ages (this study; Figs 1c and 3). Series I comprises lavas younger than 1 Ma, volcanic rocks of series II erupted between 1 and 3·5 Ma, whereas lavas of series III generally have ages between 3·5 and 5·5 Ma (Figs 1c and 2). The lavas studied here thus have similar ages to those from the western part of the HAS investigated by Weinstein *et al.* (2006), whereas many samples from the southern part of the HAS have significantly older ages (Ilani *et al.*, 2001; Shaw *et al.*, 2003). The three lava series that have been mapped also show different chemical compositions. Generally, the youngest series I lavas are alkali basalts and most series II lavas are basanitic and tephritic whereas series III ranges from mainly alkali basalts to basanites, including rare evolved lavas of trachytic and phonolitic composition (Fig. 3).

Geochemical composition

Major and trace element abundances

The lavas span a range of MgO concentrations between 11·4 and 0·2 wt % with Mg-numbers varying from 0·67 to 0·09; however, evolved lavas occur only in series III. The HAS basalts show large variations in major element compositions (Fig. 4), but within each series the relatively

Table 4: Incremental heating $^{40}Ar/^{39}Ar$ analyses on groundmass separates from Syrian volcanic rocks

Matrix step-heating		Analysis type	Age spectrum plateau age				Total gas age	Inverse isochron analysis		
Sample	Mass (μg)		Age ± 1σ (Ma)	^{39}Ar (%)	MSWD	*n* (*N*)	Age ± 1σ (Ma)	Age ± 1σ (Ma)	$^{40}Ar/^{36}Ar \pm 1\sigma$ intercept	MSWD
SY-203	5704	HR-IHA	3·40 ± 0·09	100	1·0	20(20)	3·37 ± 0·11	3·28 ± 0·15	299·4 ± 3·3	0·84
SY-203 (rpt.)	6690	HR-IHA	3·21 ± 0·08	100	1·5	20(20)	3·28 ± 0·11	3·03 ± 0·23	300·5 ± 5·0	1·45
		Combined	**3·30 ± 0·06**							
SY-224	4852	HR-IHA	**4·19 ± 0·12**	83·7	0·82	14(20)	4·61 ± 0·16	3·83 ± 0·32	298·4 ± 1·7	1·54

HR-IHA, high-resolution incremental heating analyses; rpt., duplicate step-heating analyses on same sample; Combined, weighted average of duplicate runs. Reported $^{40}Ar/^{39}Ar$ dates are weighted age estimates and errors (1σ) including uncertainties in the J-value (~0·08%). MSWD, mean square weighted deviates for plateau ages and inverse isochrons calculated for $N-2$ degrees of freedom. *N*, total number of heating steps; *n*, number of heating steps in plateau comprising per cent fraction of cumulative ^{39}Ar release. Values in bold are accepted ages based on single incremental heating analysis plateaux or weighted means from two duplicate runs.

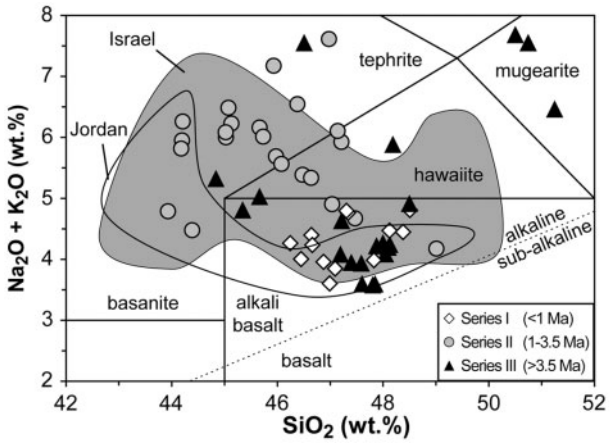

Fig. 3. Classification of the lava samples in the TAS diagram after Le Bas *et al.* (1986) with alkaline–sub-alkaline magma series discrimination after MacDonald (1968). It should be noted that series III also includes lavas with evolved compositions (one phonolite, two trachytes) that are not shown in the diagram. Also shown are fields for Pliocene to Pleistocene lavas from the Israeli part of the HAS (Weinstein *et al.*, 2006) and for Miocene to Pleistocene lavas from the Jordanian part of the HAS (Shaw *et al.*, 2003).

primitive lavas show slight increases in SiO_2, Na_2O and K_2O concentrations with decreasing MgO. These elements strongly increase in lavas with MgO contents < 5 wt %. In addition, whereas TiO_2 and CaO and also P_2O_5 concentrations are relatively constant or increase slightly between 12 and 5 wt % MgO they sharply decrease for MgO concentrations below 5 wt %. Al_2O_3 contents are similar in rocks from different lava series at a given MgO and increase throughout the whole differentiation sequence. The series II lavas with MgO >6 wt % generally have lower SiO_2 and higher TiO_2, Na_2O and K_2O as well as high P_2O_5 contents compared with the other HAS lava series (Fig. 4). However, series III is heterogeneous, with two primitive samples resembling the basanitic–tephritic series II. Series I basalts with more than 8 wt % MgO have slightly lower SiO_2 contents than the most primitive series III lavas, and the most primitive lavas of series I have higher TiO_2 contents at a given MgO concentration. These chemical differences hint at more than one petrogenetic process controlling the range of variations and indicate that the petrogenesis of the Syrian HAS lavas changed with time.

Compatible trace elements such as Ni and Cr are positively correlated with MgO (Fig. 5a and b) and series III lavas with more than 7 wt % MgO have higher Cr concentrations than primitive lavas from the other groups (Fig. 5b). Slightly negative correlations between Sc and MgO can be observed in series I and II lavas, whereas lavas of series III show no correlation (Fig. 5c). Sr correlates negatively with MgO and most of the series II lavas have higher Sr contents than the lavas of series I and II (Fig. 5d), which is in agreement with their more alkaline composition (Figs 3 and 4).

In Fig. 6a–c primitive mantle-normalized trace element patterns of the Syrian HAS series are shown. The lavas of all series are enriched in highly incompatible elements and the basanites generally are more enriched than the alkali basalts and hawaiites. The patterns of the three lava series resemble each other and, with the exception of the most evolved rocks, all the lavas show prominent positive anomalies in Ba and Sr, and negative anomalies in Th, U, K and Y. The trachyte patterns have large negative anomalies for Sr, P and Ti, and positive anomalies for Pb, Zr and Hf (Fig. 6c). Slight positive Pb anomalies are also observed for some series III basalts. The HAS samples exhibit a rough positive correlation between Ce/Pb and Nb/U ratios (Fig. 7a), which have been shown to be different

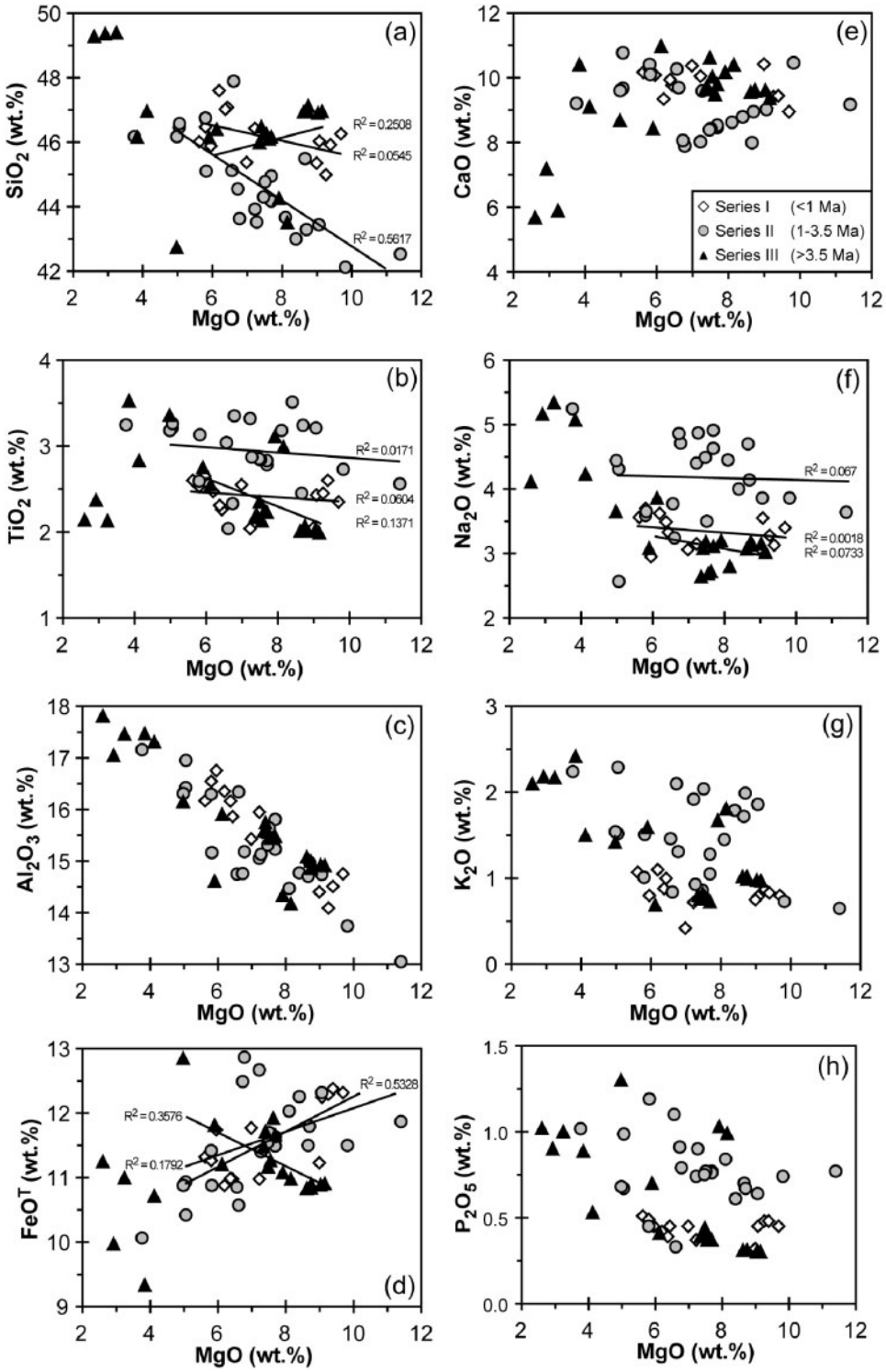

Fig. 4. Variations of selected of major elements vs wt % MgO for the Syrian sample suites: (a) SiO_2; (b) TiO_2; (c) Al_2O_3; (d) FeO^T; (e) CaO; (f) Na_2O; (g) K_2O; (h) P_2O_5. Evolved lavas, phonolite and trachytes, which are restricted to series III, are not shown. Additionally shown are regression lines for the HAS series. The regression lines include only lavas with MgO >5 wt %, and were used to correct for fractional crystallization.

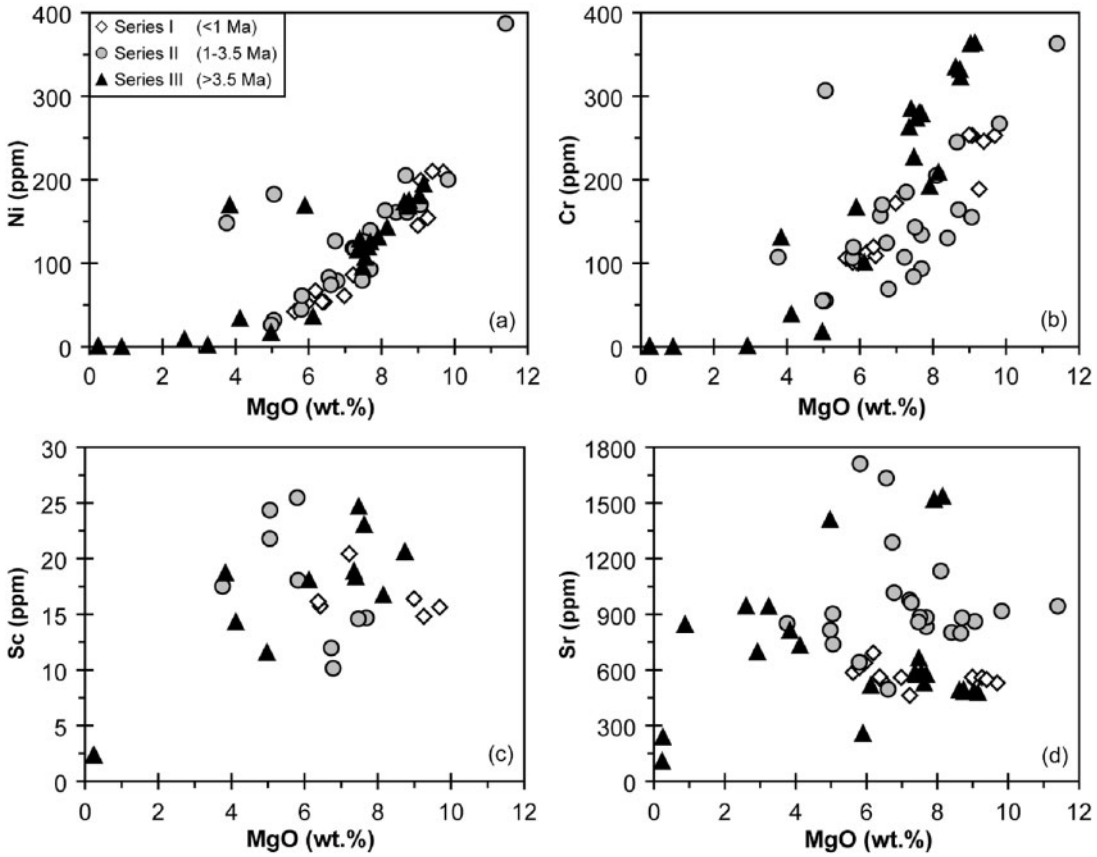

Fig. 5. Variations of selected trace elements vs wt % MgO for the Syrian lavas: (a) Ni; (b) Cr; (c) Sc; (d) Sr.

and relatively constant for rocks formed from the Earth's mantle and continental crust (Hofmann *et al.*, 1986). Although a few lavas tend to lower values resembling average continental crust, most samples have Ce/Pb similar to the range suggested for oceanic basalts (Hofmann *et al.*, 1986). In a plot of Th/U vs Rb/Cs most of the HAS lavas fall well within the range of mantle-derived melts, although one sample from series I has a distinct low Th/U ratio (Fig. 7b). The K/La ratios of the Syrian volcanic rocks show a rough negative correlation with $(La/Sm)_N$ and the most enriched basalts from series II and III have the lowest K/La (Fig. 7c). Whereas the K/La ratios of series II and III lavas are highly variable, series I samples show a much more restricted range. The trachytes lie outside the basalt trend at high K/La and $(La/Sm)_N$ (Fig. 7c). The HAS lavas show a negative correlation between Ce/Pb and K/La similar to samples from Jordan and Israel (Fig. 7d).

Isotopic compositions

The Syrian series II and III HAS volcanic rocks show a negative trend between Sr and Nd isotope ratios whereas the series I samples have lower $^{143}Nd/^{144}Nd$ than series III lavas at a $^{87}Sr/^{86}Sr$ of 0·7033 (Fig. 8a). The series II and III lavas show the same trend of Sr and Nd isotope ratios as the lavas from the Jordanian part of the HAS (Bertrand *et al.*, 2003; Shaw *et al.*, 2003). In contrast, the series I lavas resemble the lavas from the western edge of the HAS in Israel (Weinstein *et al.*, 2006) and two lavas previously analysed (Bertrand *et al.*, 2003). On a larger scale, the Syrian HAS lavas also mostly overlap with the field of Saudi Arabian lavas, which are highly variable (Fig. 8b). All Syrian HAS basalts have lower $^{87}Sr/^{86}Sr$ ratios for a given $^{143}Nd/^{144}Nd$ ratio and higher $^{206}Pb/^{204}Pb$ than the Afar plume lavas with high $^{3}He/^{4}He$ (Fig. 8b, g and h). The series II samples are similar to Red Sea mid-ocean ridge basalt (MORB) in terms of their Pb isotope compositions (Fig. 8d and f) and are also relatively MORB-like in Sr and Nd isotope composition (Fig. 8b). In contrast, the lava series I and III show much higher $^{207}Pb/^{204}Pb$ (Fig. 8d) and $^{87}Sr/^{86}Sr$ ratios than Red Sea MORB (Fig. 8b and g).

Most Syrian HAS lavas lie on a positive trend of $^{87}Sr/^{86}Sr$ vs Ba/Nb with the series II samples lying at the lower end and two series III samples at the end with high

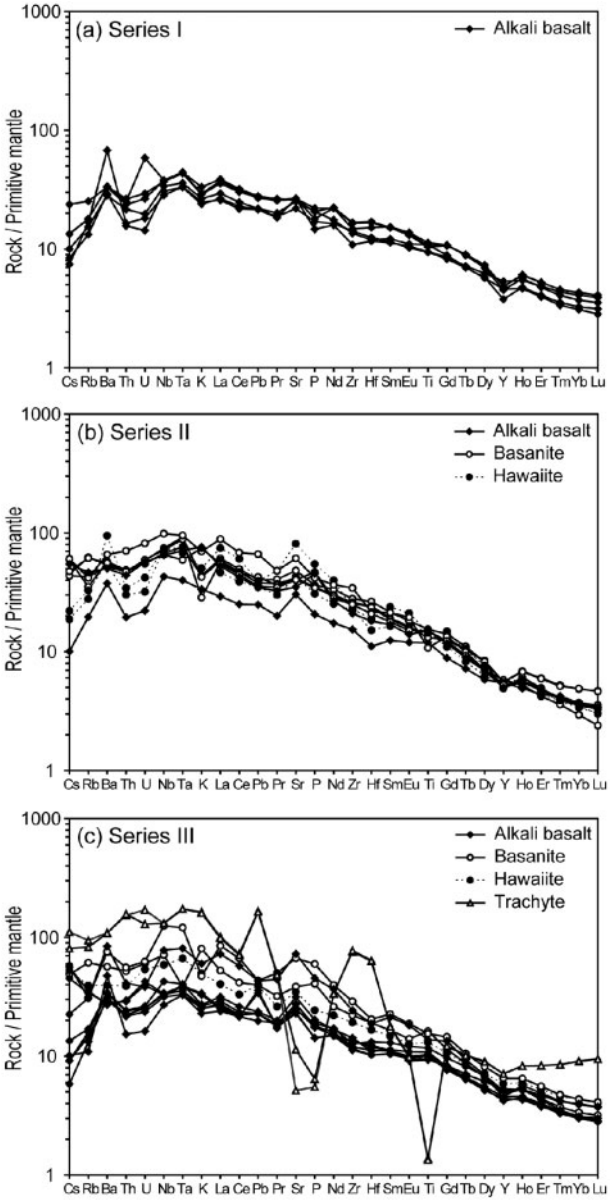

Fig. 6. Primitive mantle-normalized trace element diagrams showing the compositions of (a) series I, (b) series II, and (c) series III lavas. Primitive mantle normalizing composition is from Sun & McDonough (1989).

Ba/Nb and Sr isotope ratios (Fig. 9a). Two series III samples have much higher $^{87}Sr/^{86}Sr$ at intermediate Ba/Nb. In Fig. 9b the Nd isotopic compositions of the HAS lavas are plotted against $(La/Sm)_N$; the data define a rough positive correlation in which series I lavas lie at the low end and series II lavas at the end with high $(La/Sm)_N$ and $^{143}Nd/^{144}Nd$. Compared with Red Sea lavas and with Afar plume related lavas the investigated samples have generally higher $(La/Sm)_N$, but are similar to the Jordanian HAS lavas.

DISCUSSION

Effects of alteration

During weathering of rocks elements such as K, Rb, Cs, U or Ba can be mobilized by aqueous fluids, leading to both (1) either the addition or subtraction of these elements from the rock and (2) increasing H_2O and CO_2 contents as expressed by elevated loss on ignition (LOI) values. However, the HAS lavas are usually fresh and show only alteration of olivine to iddingsite and a few calcite amygdules. Except for two samples with high LOI values (2·7 and 3·7 wt %) the LOI content generally lies below 2 wt %, which is typical for alkaline lavas (Table 2). In addition, most of the lavas have Nb/U ratios similar to or lower than those of oceanic basalts (Fig. 7a) and show Th/U and Rb/Cs ratios within the range representative for mantle-derived magmas (Fig. 7b), which indicates that they have not been significantly affected by alteration. Thus, alteration processes appear to have had only a minor effect, even on the mobile element contents of the HAS lavas.

Control of fractional crystallization and crystal accumulation on HAS lavas

The abundance of phenocryst phases, as well as the wide range of MgO contents and Mg-numbers of the samples, implies crystal fractionation during magma ascent (Figs 4 and 5). However, the large variations in the concentrations of incompatible elements such as K (Fig. 4g) and in incompatible element ratios such as $(La/Sm)_N$ (Fig. 7c) imply that the lavas within each series (except series I) are not cogenetic. Instead, the magmas of series II and III must have formed from different source compositions, variable degrees of partial melting, or crustal contamination processes. Throughout the differentiation sequence the volcanic series are influenced by crystallization of olivine, clinopyroxene, spinel and, at later stages, apatite, whereas minor feldspar fractionation is restricted to the most evolved lavas. Olivine is one of the major fractionating phases and its extraction is indicated by decreasing Ni and MgO contents (Fig. 5a). In contrast, the most primitive sample SY-272, with a Mg-number of 0·67, has a high Ni content (387 ppm) and a high Ni/Cr ratio (1·07), but shows comparable trace and major element concentrations to the other lavas (Table 2), suggesting olivine accumulation. This assumption is also confirmed by the occurrence of olivine xenocrysts in thin section and the observed mantle xenolith with strongly resorbed olivines and orthopyroxenes may represent a dissolved peridotite (wehrlite). Decreasing Cr contents at a MgO concentration of about 9 wt % indicate spinel fractionation (Fig. 5b). The negative correlation between Sc and MgO contents and the relatively constant CaO/Al_2O_3 (not shown) in the lavas with MgO >5 wt % indicate that clinopyroxene fractionation plays no major role in the

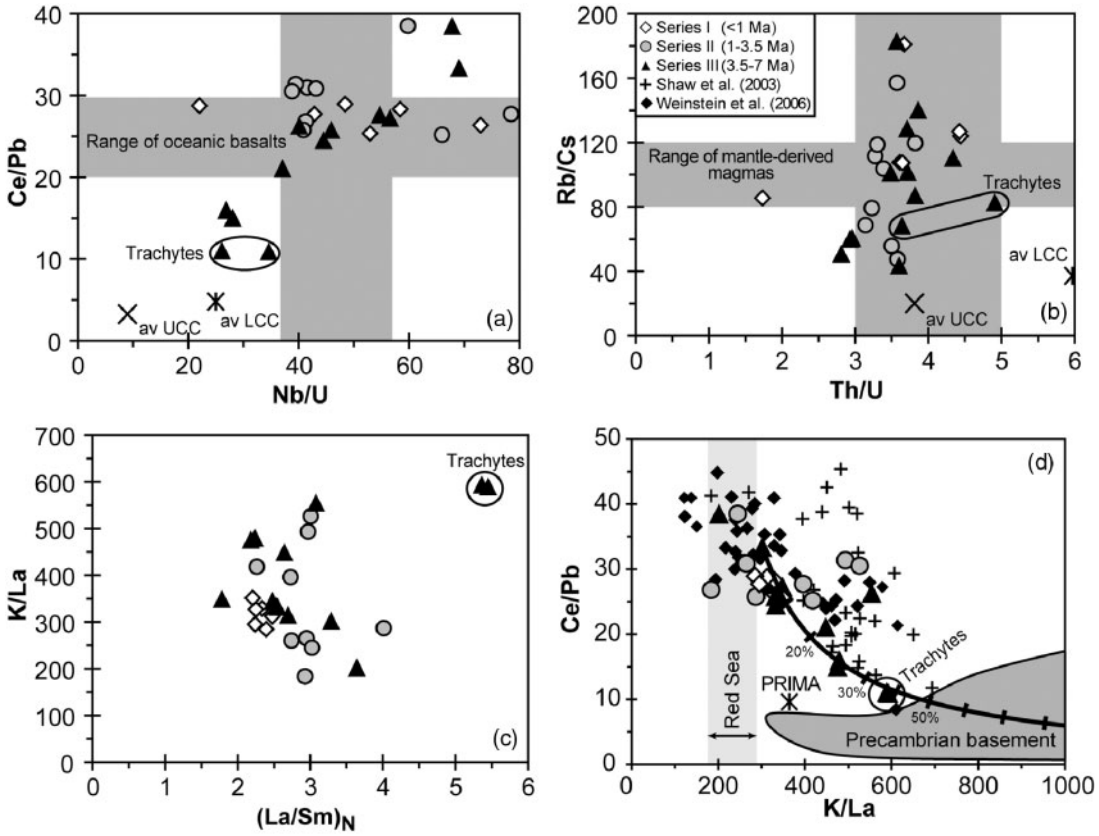

Fig. 7. (a) Variation of Nb/U vs Ce/Pb. Grey fields are defined based on studies of oceanic basalts (Hofmann *et al.*, 1986) which are not affected by continental crustal contamination. (b) Variations of Th/U vs Rb/Cs. Grey fields show the range representative for mantle-derived magmas. (c) Chondrite-normalized La/Sm vs K/La for the Syrian lavas. (d) Variation of K/La vs Ce/Pb. Additional fields show the composition of the Precambrian basement (Jarrar *et al.*, 2003) and the K/La range of Red Sea island alkali basalts (Rogers, 1993). Also shown is a bulk mixing curve between sample SY-224 and the Precambrian basement as given by Jarrar *et al.* (2003); the tick marks on the mixing curve indicate 10% intervals. Chondrite values are from McDonough & Sun (1995) and average compositions of upper (UCC) and lower (LCC) continental crust in (a) and (b) are from Rudnick & Fountain (1995).

differentiation of series I and II lavas, but appears to be more prominent in series III lavas as the Sc concentrations and CaO/Al_2O_3 decrease with decreasing MgO (Fig. 5c). The increasing Al_2O_3 and Sr concentrations with decreasing MgO as well as the lack of Eu anomalies (Fig. 6) imply that plagioclase fractionation did not play a role in the early stages of differentiation. Between MgO concentrations of 12 and ~5 wt % olivine and spinel fractionation clearly dominate over clinopyroxene removal and the inflection of CaO at a MgO of ~5 wt % probably indicates a significant increase of the relative proportion of clinopyroxene fractionation as compared with olivine and spinel removal. Concerning the more evolved rocks of series III, the crystallization of titanomagnetite is responsible for the lower FeO^T and TiO_2 contents in samples with MgO below 5 wt %. The P_2O_5 decrease starting at 5 wt % MgO is caused by apatite fractionation. Only the most evolved rocks of series III show some evidence for feldspar removal, as indicated by their comparatively low Al_2O_3 and Sr concentrations and their pronounced negative Eu anomalies (Fig. 6c).

Crustal contamination of the HAS magmas

Magmas rising through the continental lithosphere often stagnate at crustal levels and assimilate crustal material. Mid-ocean ridge and ocean island basalts have average Nb/U ratios of 47 ± 10 and average Ce/Pb ratios of 25 ± 5, reflecting the composition of the Earth's mantle, whereas the continental crust has characteristically low Nb/U and Ce/Pb ratios (Hofmann *et al.*, 1986). The high mantle-like Nb/U and Ce/Pb values of most HAS lavas imply negligible crustal contamination (Fig. 7a). However, several series III lavas have Nb/U and Ce/Pb ratios lower than the range typical for oceanic lavas, which suggest the involvement of crustal contamination (Fig. 7a). The trachytes represent the most evolved lavas and have the lowest Nb/U and Ce/Pb ratios, which imply that assimilation and crystal

fractionation plays a major role in their petrogenesis. The HAS lavas from this study as well as those from the parts in Jordan and Israel lie on a negative trend of K/La vs Ce/Pb; the rocks with low Ce/Pb resemble the compositions of some of the Precambrian basement rocks (Fig. 7d). Bulk mixing calculations between the most primitive Syrian samples and the Precambrian basement rocks reveal that contamination of the magmas with about 30–40% of an upper crustal component can account for low Ce/Pb coupled with high K/La ratios as observed in the most evolved rocks of series III (Fig. 7d).

Because isotopic compositions are not influenced by crystal fractionation or the degree of partial melting, the Sr and Nd isotopic array of the HAS lavas implies that at least three isotopically distinct end-members are involved in their petrogenesis (Fig. 8a and b). The lavas (alkali basalts) with the highest $^{87}Sr/^{86}Sr$ have crust-like Nb/U and Ce/Pb and trend towards the $^{207}Pb/^{204}Pb$ and $^{208}Pb/^{204}Pb$ compositions of crustal rocks from Yemen (Fig. 8d and f). Thus, some of the Syrian series III lavas appear to have assimilated crustal material leading to high $^{87}Sr/^{86}Sr$, $^{206}Pb/^{204}Pb$ and $^{207}Pb/^{204}Pb$ isotope ratios and to low $^{208}Pb/^{204}Pb$ similar to compositions observed in HAS lavas from Jordan (Shaw *et al.*, 2003) (Fig. 8). Shaw *et al.* (2003) postulated that the lavas of the Jordan part of HAS have assimilated up to 20% of Late Proterozoic crust during their ascent to the surface; these have low $^{208}Pb/^{204}Pb$ ratios for a given $^{206}Pb/^{204}Pb$ when compared with the Syrian lavas (Fig. 8f). On the basis of Sr and Nd isotope compositions, Weinstein *et al.* (2006) suggested that a crustal contribution to the Israeli magmas is small and probably restricted to a lower crustal component. However, the lavas from the northwestern part of the HAS in Israel (Weinstein *et al.*, 2006) also lie on the negative trend between K/La vs Ce/Pb, with one sample having a Ce/Pb value of 8·5, and thus assimilation of crustal material appears likely (Fig. 7d). We conclude that crustal contamination is an important process affecting the geochemical and isotope compositions of many lavas from the HAS volcanic field, most clearly those from the northern and eastern part of the basaltic plateau (i.e. in Jordan and Syria).

Magma generation in the mantle beneath the HAS volcanic field

Primitive magma compositions and partial melting processes beneath the HAS

Crystal fractionation and crustal assimilation processes have modified the Syrian lavas and, thus, no primary magmas from the mantle have been sampled. To compare the differences in magma genesis we have corrected the effects of fractional crystallization on the major elements SiO_2, Na_2O and TiO_2 to MgO contents of 9 wt % following the approach of Klein & Langmuir (1987) and using the regression lines shown in Fig. 4. Not included in the fractionation correction were crustally contaminated samples; that is, those lavas falling outside the range of mantle compositions in terms of Nb/U and Ce/Pb (Fig. 7a) and lavas with MgO concentrations below 5 wt %, because of their complex fractionation history. We find that lava series II has the highest fractionation-corrected Na_2O ($Na_{9.0}$) and $Ti_{9.0}$ but the lowest $Si_{9.0}$ and a negative correlation between $Si_{9.0}$ and $(Dy/Yb)_N$ (Fig. 10). The differences in fractionation-corrected major element and heavy REE (HREE) composition imply that the series II lavas formed by lower degrees of melting than magmas of the other two series, probably also at higher pressures; that is, they may represent melts from the deeper part of the melting column. Depending on the mantle composition, the degree of melting can be determined, and is about 4–6% for series II magmas and 6–12% for the series I and III lavas, with the oldest series III magmas representing the highest degree melts if we assume an enriched garnet peridotite source relative to a primitive mantle composition (Fig. 10a). Similar results can be obtained when the degree of melting is calculated on the basis of REE contents in crustally uncontaminated primitive Syrian lavas. As shown in Fig. 11, the high $(La/Sm)_N$ ratios and incompatible element concentrations of the HAS samples cannot be modelled with a source of primitive mantle composition but require melting of an enriched mantle. Because the relatively high Nd isotope ratios of the most primitive magmas suggest that their mantle sources had been depleted for a long period of time (Fig. 8a) we used in our model a re-enriched source composition representing 15% of a 2·5% melt from a primitive mantle that was previously depleted by 0·5% melting. In agreement with Shaw *et al.* (2003) we find no evidence for melting solely in the spinel stability field because melting of neither a primitive mantle composition nor an enriched mantle source can reproduce the high REE ratios of the Syrian lavas (Fig. 11). However, our model does not require mixing of melts from garnet peridotite with melts from spinel peridotite and instead we suggest that melting occurred only in garnet peridotite facies mantle. This is supported by (1) the nearly constant Yb concentrations indicating buffering by garnet, (2) the very high $(Sm/Yb)_N$ and $(Dy/Yb)_N$ ratios, and (3) the thickness of the lithosphere of 75–80 km, which is close to the spinel-out reaction boundary for relatively fertile mantle (Fig. 12). We agree with Shaw *et al.* (2003) that the linear data trends in Fig. 11 could reflect binary mixing, which is also indicated by the radiogenic isotopes (Fig. 8); the two melts probably form by different degrees of melting from two different sources within the garnet stability field. In agreement with our model of the Na and Ti contents, the range of REE ratios described by the uncontaminated Syrian HAS lavas indicates that the most primitive lavas of series II were formed by about 3–6%

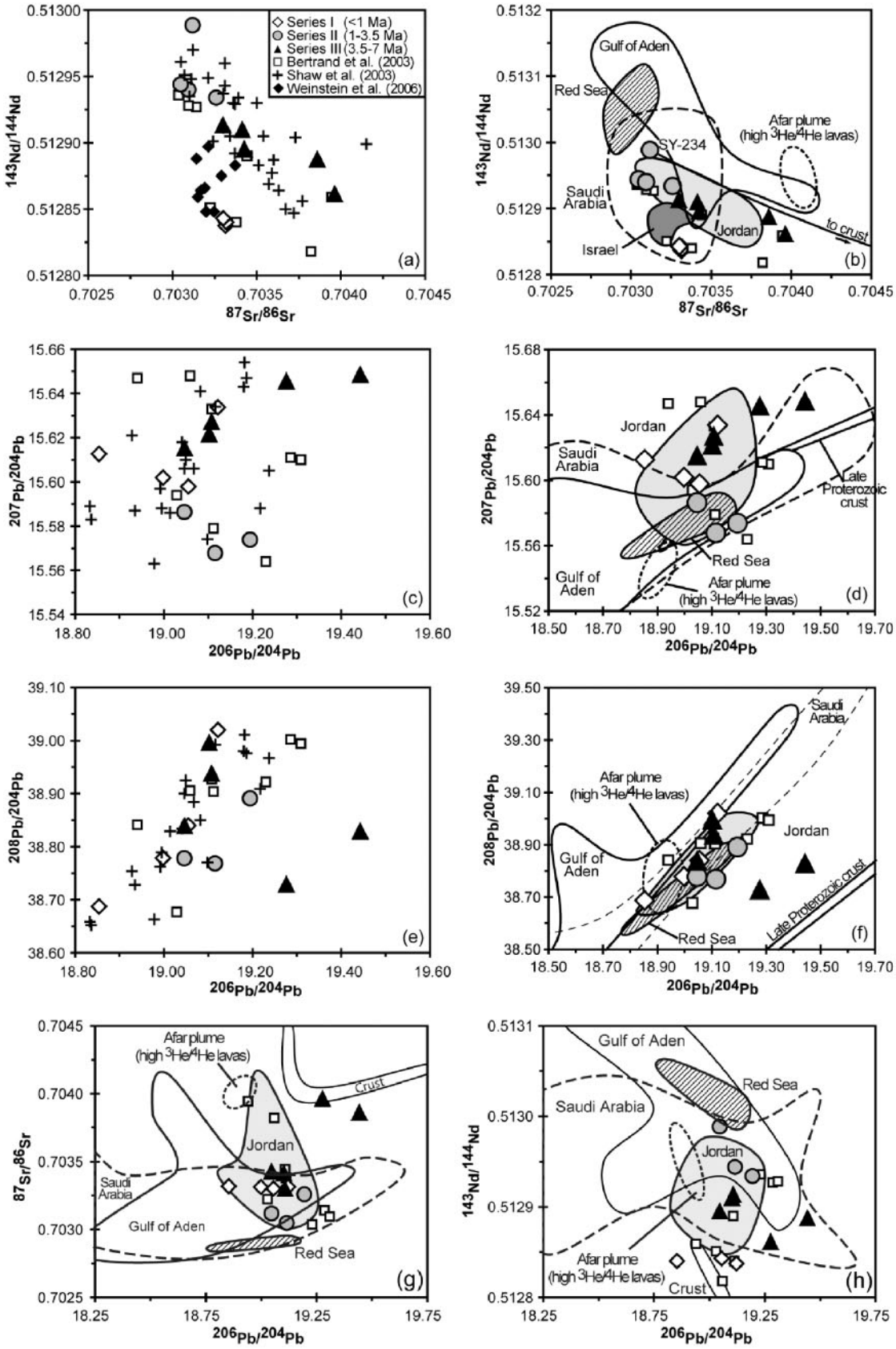
Series I (<1 Ma)
Series II (1-3.5 Ma)
Series III (3.5-7 Ma)
Bertrand et al. (2003)
Shaw et al. (2003)
Weinstein et al. (2006)
(a)
143Nd/144Nd
87Sr/86Sr
Gulf of Aden
Red Sea
Afar plume (high 3He/4He lavas)
SY-234
Saudi Arabia
Jordan
Israel
to crust
(b)
207Pb/204Pb
206Pb/204Pb
(c)
Late Proterozoic crust
(d)
208Pb/204Pb
(e)
Crust
(f)
(g)
(h)

melting of an enriched garnet lherzolite, whereas most of the primitive lavas of series I and III were generated by larger degrees of partial melting of about 8–12% (Fig. 11).

None the less, differences in the degree of melting at different depths can account for variable incompatible element concentrations in both the primitive and fractionation-corrected samples (e.g. Ti, P; Figs 4 and 10). Melting experiments on natural dry lherzolites have shown that the SiO_2 contents of primary tholeiitic to alkali basaltic melts mainly reflect the pressure of melt formation; increasing pressures lead to decreasing SiO_2 in the melt (Hirose & Kushiro, 1993). Applying the algorithm developed by Haase (1996) on the basis of experiments on dry peridotite to estimate the average pressures of melting of the primary HAS magmas, as achieved by addition of olivine to primitive magma compositions, suggests that series I and III could be derived from similar depths of about 100 km (Fig. 12). Magma generation at this depth is in accordance with the low seismic velocities observed at about 100 km depth beneath Syria (Debayle *et al.*, 2001; Daradich *et al.*, 2003) and with the seismically and petrologically determined thickness of the Arabian lithosphere (McGuire & Bohannon, 1989; Nasir & Safarjalani, 2000).

Applying the algorithm for pressure estimations to primary series II magmas, melt formation would have taken place at depths of about 140 km (Fig. 12). These abrupt changes in melting depths (from shallow to deep to shallow) over a relative short time span of about 2·5 Myr (i.e. during the eruption of the three HAS series) cannot easily be explained. However, the algorithm developed by Haase (1996) takes into account only those experiments that were carried out under dry conditions (i.e. no volatiles or hydrous minerals were present), and thus the use of the algorithm is not appropriate when melting is assumed to be wet, and would lead to an overestimation of the melting pressure. In this context it has been shown that highly undersaturated magmas with SiO_2 <45 wt % similar to series II lavas probably form in the presence of CO_2 (e.g. Eggler, 1978; Wyllie, 1978), requiring relatively high CO_2 contents in the mantle source of the series II magmas. Hirose (1997), for example, concluded on the basis of diamond aggregate melting experiments that nephelinitic to basanitic magmas form at 3 GPa and >1475°C in the presence of CO_2 rather than being the product of high-temperature melting above 3 GPa. Thus, experimental constraints suggest that the basanites of series II could form from a volatile-rich garnet peridotite mantle source at about 100 km depth (Fig. 12), compatible with the strongly fractionated REE patterns observed in the series II magmas (Fig. 11).

McKenzie & Bickle (1988) demonstrated that decompressional melting of the asthenosphere with a potential temperature of 1280°C requires a stretching factor of the lithosphere in the range of 2–5. However, no significant extensional tectonic features (e.g. the formation of graben structures and significant thinning of the lithosphere) can be related to the volcanism at this time and tectonic movements are limited to the Dead Sea fault system (e.g. Heimann & Ron, 1993; Brew *et al.*, 2001b). Melting of dry mantle peridotite at 90–100 km depth requires

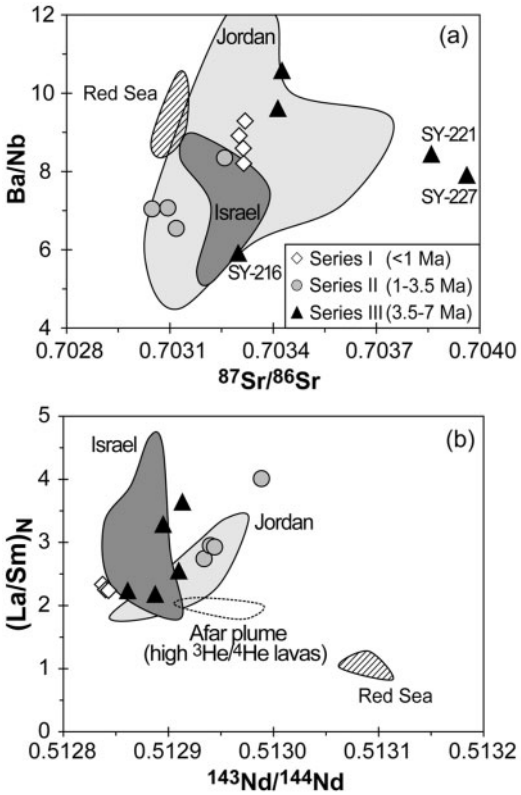

Fig. 9. (a) $^{87}Sr/^{86}Sr$ vs Ba/Nb. (b) $^{143}Nd/^{144}Nd$ vs chondrite-normalized La/Sm for the Syrian lavas. Chondrite composition for normalization is from McDonough & Sun (1995). Data sources for additional fields as in Fig. 6.

Fig. 8. (a and b) Sr vs Nd isotopic compositions of the HAS lavas. Fields and data points are representative of contemporaneous volcanic rocks from Jordan (Bertrand *et al.*, 2003; Shaw *et al.*, 2003), Israel (Weinstein *et al.*, 2006), the Red Sea (Eissen *et al.*, 1989; Haase *et al.*, 2000), the Afar plume lavas with high $^3He/^4He$ ratios (Pik *et al.*, 1999), Gulf of Aden (Schilling *et al.*, 1992) and Saudi Arabia (Hegner & Pallister, 1989; Altherr *et al.*, 1990; Bertrand *et al.*, 2003). Additional data for the Syrian HAS volcanic field are from Bertrand *et al.* (2003). Line in (b) represents a bulk mixing curve between primitive basalt sample SY-234 and average Proterozoic crust [data from Hegner & Pallister (1989)]. (c and d) $^{206}Pb/^{204}Pb$ vs $^{207}Pb/^{204}Pb$ and (e and f) $^{206}Pb/^{204}Pb$ vs $^{208}Pb/^{204}Pb$ ratios of the HAS lavas. (g and h) $^{206}Pb/^{204}Pb$ vs $^{87}Sr/^{86}Sr$ and $^{143}Nd/^{144}Nd$. Compositions of Late Proterozoic crustal rocks in (c) are from Baker *et al.* (2000).

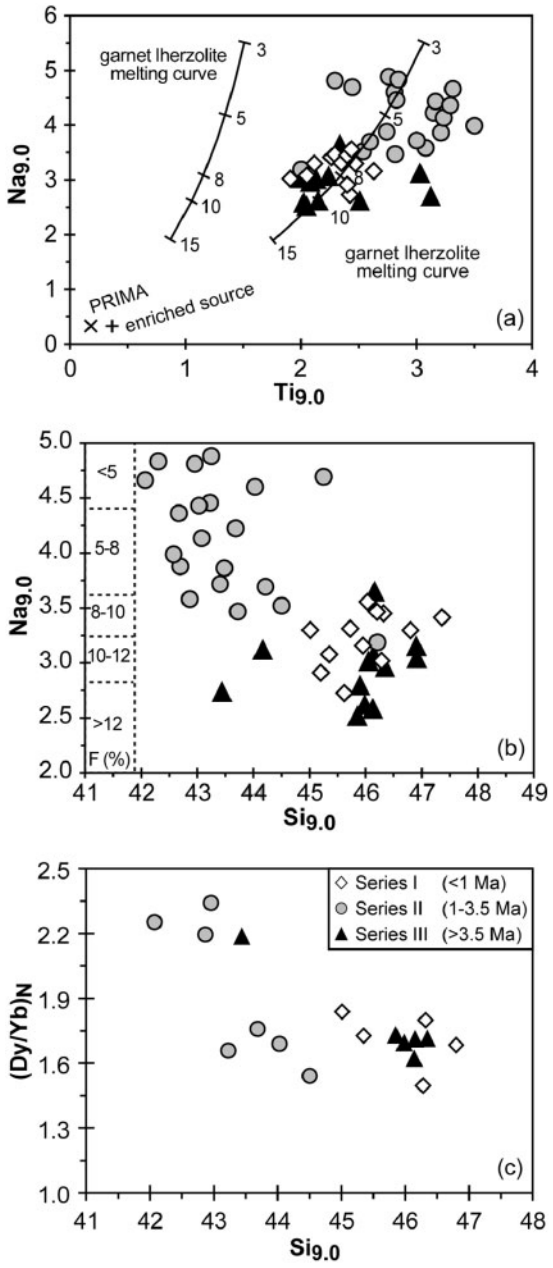

Fig. 10. (a) Fractionation-corrected Ti ($Ti_{9.0}$) and Na ($Na_{9.0}$) concentrations in the Syrian lavas. Also shown are melting curves for non-modal batch melting of a garnet lherzolite; the numbers give the degree of melting in per cent (F). Garnet lherzolite composition: 0·598 olivine, 0·076 clinopyroxene, 0·211 orthopyroxene, 0·115 garnet. The mantle source concentrations for the primitive mantle (PRIMA) are Ti 0·18 wt % and Na 0·33 wt %, and for the enriched mantle are Ti 0·37 wt % and Na 0·33 wt %. Distribution coefficients used are from Onuma *et al.* (1968), Leeman & Scheidegger (1977), Hart & Dunn (1993) and Suzuki *et al.* (2000). (b) $Si_{9.0}$ vs $Na_{9.0}$. Fields with numbers correspond to the amount of melting (F) calculated on the basis of Na concentrations using experimental data for peridotite KLB-1 from Hirose & Kushiro (1993). A regression through the data from their experimental study gives the relationship $F\ (\%) = -0{\cdot}1568\ \ln(Na_2O) + 0{\cdot}2818$ with a correlation factor $R^2 = 0{\cdot}918$. This algorithm was used to calculate the extent of melting needed to generate the HAS lavas. (c) $Si_{9.0}$ vs chondrite-normalized Dy/Yb ratios for the HAS lava series. Primitive mantle composition and chondrite values are from McDonough & Sun (1995).

a potential mantle temperature increased by about 150°C (Fig. 12). Following the empirical algorithm of Albarède (1992), the temperatures of the primary magmas at about 100 km depth are calculated to be 1457°C, 1504°C and 1429°C for series I, II and III, respectively (Fig. 12). These temperatures are ~50–150°C higher than the average potential mantle temperature of ~1300°C (McKenzie & Bickle, 1988), and fall into the range of excess temperatures thought to be characteristic for the presence of mantle plumes (e.g. White & McKenzie, 1989). An increased temperature of the upper mantle beneath Syria is likely because (1) seismic tomography shows lower seismic velocities (Debayle *et al.*, 2001; Daradich *et al.*, 2003), (2) mantle xenoliths suggest an increased geothermal gradient in the mantle beneath the Arabian volcanic fields (Camp & Roobol, 1992; Snyder *et al.*, 1993), and (3) the region beneath the HAS volcanic field is uplifted by ~2000 m (Brew *et al.*, 2000, 2001*a*). In agreement with previous workers (Shaw *et al.*, 2003; Weinstein *et al.*, 2006) we conclude that the voluminous melting within the HAS province is a consequence of elevated mantle temperatures beneath this part of the Arabian Plate. The melting conditions of the HAS lavas are consistent with the formation of the silica-undersaturated lavas of series II, with ages between 3·5 and 1 Ma, by lower degrees of melting of a volatile-rich mantle source, and with the derivation of the youngest lavas of series I, as well as the lavas older than 3·5 Ma of series III, by relatively large degrees of melting of mantle material with a significant excess temperature (i.e. from a mantle plume). The process of mantle upwelling is probably young and started in the Miocene, at a time similar to or somewhat before the onset of volcanic activity, because the Paleogene sediments are unconformably overlain by the HAS lavas.

Mantle sources of the Syrian HAS magmas

Shallow melting of the lithospheric mantle?

Variable depths of partial melting were also suggested by Shaw *et al.* (2003) and Weinstein *et al.* (2006), who proposed that the early alkali basaltic magmas formed by relatively shallow melting of the lithospheric mantle, whereas the later highly undersaturated magmas may have formed deeper in the asthenosphere. Interestingly, those workers did not find evidence for a late shallow and higher degree melting phase comparable with the series I lavas. The presence of these lavas in the Syrian part of the HAS is difficult to explain by a transition from lithospheric to asthenospheric melting caused by progressive lithospheric thinning, because melting processes in this late stage resemble those for the earliest lavas. Furthermore,

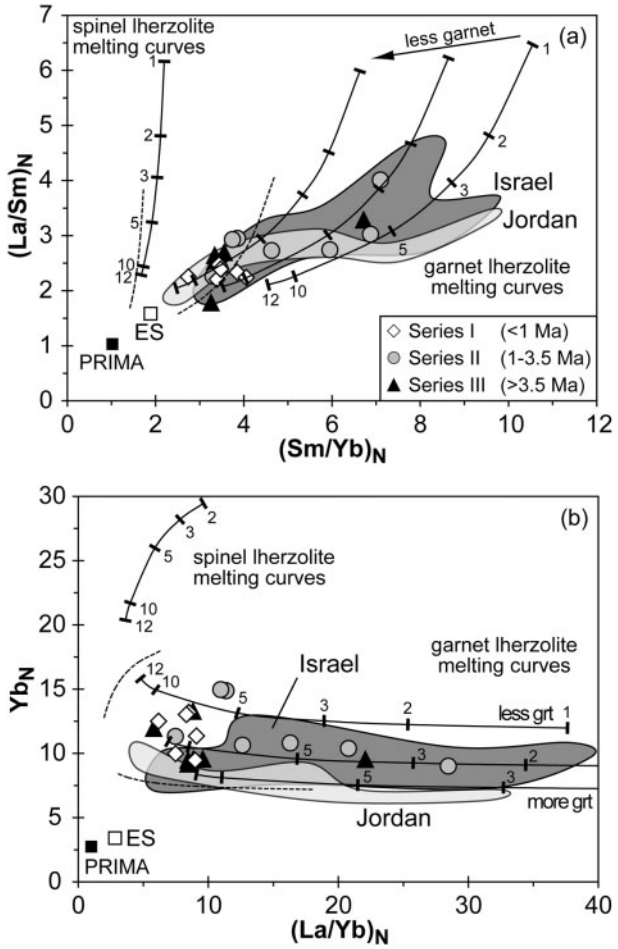

Fig. 11. Diagrams of chondrite-normalized (a) Sm/Yb vs La/Sm and (b) La/Yb vs Yb for uncontaminated Syrian HAS lavas. Additionally, data fields are from Weinstein *et al.* (2006) and Shaw *et al.* (2003) for the Israeli and Jordanian HAS lavas, respectively. Also shown are melting curves for non-modal batch melting of garnet and spinel lherzolites of PRIMA compositions (dashed lines) and enriched source compositions (representing mantle enriched with 15% of a 2·5% melt from 0·5% depleted mantle of PRIMA composition) with variable amounts of garnet (continuous lines); the numbers give the degree of melting (F). Garnet lherzolite composition: 0·552 olivine, 0·202 clinopyroxene, 0·212 orthopyroxene, 0·04 garnet. Melting proportions of garnet lherzolite: 0·633 olivine, 0·203 clinopyroxene, 0·113 orthopyroxene, 0·05 garnet. Spinel lherzolite composition: 0·53 olivine, 0·17 clinopyroxene, 0·27 orthopyroxene, 0·030 spinel. Melting proportions of spinel lherzolite: 0·63 olivine, 0·20 clinopyroxene, 0·11 orthopyroxene, 0·05 spinel. Assumed enriched mantle source (ES) concentrations: La 2·29 ppm, Sm 0·93 ppm, and Yb 0·55 ppm. Distribution coefficients used are from Kelemen *et al.* (1993) and are taken from Johnson (1998) for Sm and Yb between garnet and melt. PRIMA and chondrite values are from McDonough & Sun (1995).

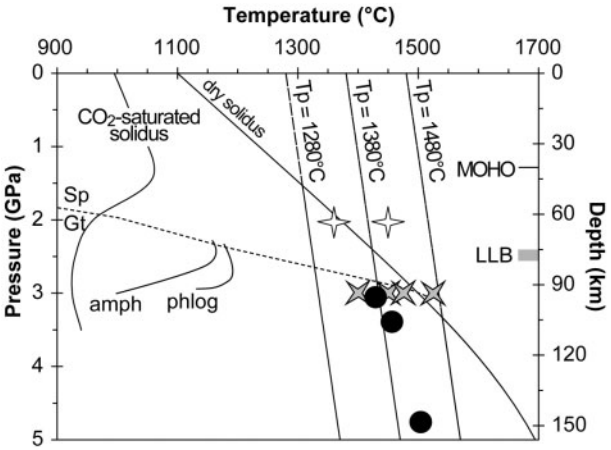

Fig. 12. Pressure–temperature (P–T) diagram showing the conditions of magma generation. P–T estimates are based on estimated primary magma compositions (•) for the HAS series. Also shown are the solidi for CO_2-saturated mantle peridotite (Falloon & Green, 1990) and dry mantle (McKenzie & Bickle, 1988), as well as a series of asthenospheric mantle adiabats (McKenzie & Bickle, 1988) for different potential mantle temperatures (1280°C, 1380°C, 1480°C). White stars are melting experiments of peridotite + CO_2 from Mysen & Kushiro (1977); grey stars are those from Hirose (1997). The spinel (Sp) to garnet (Gt) transition is shown as a dashed line and amphibole (amph) and phlogopite (phlog) stability limits as continuous curved lines based on experimental data (Robinson & Wood, 1998). Temperature estimates are based on the empirical relation T (°C) =2000 [MgO/(SiO_2 × MgO)] + 969 (Albarède, 1992) and pressure calculations are based on melting experiments using the equation P (GPa) = 23·217 − 0·4381 SiO_2 with a correlation factor R = 0·878 as cited by Haase (1996). Pressure–depth conversion is made using the relationship depth (km) = 3·02 P (kbar) + 5 (Scarrow & Cox, 1995). Crustal thickness is based on the geophysical data of Best *et al.* (1990) and McBride *et al.* (1990), and the lower lithosphere boundary (LLB) is from McGuire & Bohannon (1989).

Weinstein *et al.* (2006) attributed the low Ba/Nb and Ba/Sr in the HAS lavas relative to primitive mantle to the presence of residual amphibole in the mantle source; this would be important evidence for lithospheric melting because at pressures below 3 GPa amphibole is stable only at temperatures below 1200°C (Green, 1973; Wallace & Green, 1988). However, Ba/Nb correlates with Sr isotope composition (Fig. 9a) and the crustally uncontaminated series I and III alkali basalts (with high Ce/Pb) have K/La of 100–300, similar to the series II basanites, which in turn closely resemble alkali basalts from islands in the southern Red Sea (Fig. 7d). The Red Sea alkali basalts occur in a region of significant lithospheric thinning (estimated thickness of 30 km) and probably represent melts from a mixture of asthenospheric and Afar plume sources (Rogers, 1993). We find no evidence for the presence of residual amphibole in the source of the HAS magmas and thus no evidence for lithospheric melting. Instead, we suggest that the low Ba/Nb and K/La of the uncontaminated lavas reflects the composition of the mantle source of the HAS magmas. The compositional resemblance of the southern Red Sea alkali basalts and the HAS basanites suggests that they have a common source, which is widely distributed in the upper mantle beneath the Arabian Plate. This source probably occurs in the low-velocity zone outlined by geophysical data (Debayle *et al.*, 2001; Daradich *et al.*, 2003).

The mantle sources of the HAS lavas

Although the HAS lavas have a large range of Sr–Nd–Pb isotopic compositions and high incompatible element ratios, it is possible to define two distinct mantle end-members and one crustal contaminant (Figs 7–9). The crustal contaminant, discussed above, has high Sr and Pb isotope ratios together with low Ce/Pb and probably represents local Proterozoic upper crustal rocks. One mantle end-member is sampled preferentially by series II lavas and has a high $^{143}Nd/^{144}Nd$ of 0·5130, $^{87}Sr/^{86}Sr$ of 0·703l and relatively unradiogenic Pb isotope ratios, resembling the source of the Red Sea alkali basalts (Fig. 8). This mantle source probably represents the ambient asthenosphere, as it has low highly incompatible trace element ratios (e.g. Ba/Nb ~7) similar to MORB (Fig. 9a) and appears to produce only small-degree melts (i.e. it appears to be relatively cold). However, the mantle source of series II lavas is more enriched relative to the Red Sea MORB source in incompatible elements; for example, it has slightly higher Sr isotope ratios implying a higher Rb/Sr ratio compared with the Red Sea MORB source. Thus, the series II magmas probably formed from relatively enriched zones within the heterogeneous asthenosphere, which melt preferentially and dominate the small-degree melts such as the HAS series II and Red Sea islands alkali basalts, but which are more diluted in the Red Sea tholeiitic basalts. Because the Pb isotopic ratios of the HAS series II lavas are similar to those of Red Sea MORB this enrichment must have occurred relatively recently.

The second mantle end-member, most clearly reflected in the series I lavas, has a low $^{143}Nd/^{144}Nd$ (~0·51284) and a Sr isotope ratio of ~0·7033, but variable Pb isotope ratios with $^{206}Pb/^{204}Pb$ ranging from about 18·8 to 19·1. The crustally uncontaminated series III lavas resemble the series I samples in terms of Sr and Pb isotopes but have slightly higher $^{143}Nd/^{144}Nd$, which probably indicates that they represent mixtures between the series I and II magmas. The series I and III magmas formed by larger degrees of melting than the series II melts and thus from relatively hot mantle material (i.e. from a mantle plume source). This source is more enriched in Ba and K than the series II source because it has Ba/Nb >8 and K/La ~300 (Figs 7 and 9).

The Arabian part of the Afro-Arabian dome (Camp & Roobol, 1992) (i.e. the Arabian swell) is a large area of elevated topography, extending from Yemen in the south along western Arabia to Syria in the north, which may have formed by northward flow of material from the Afar plume (Camp & Roobol, 1992); this is consistent with: (1) the low shear-wave velocities in the mantle beneath western and northern Arabia (Debayle *et al.*, 2001); (2) the lack of agreement between mantle and near-surface temperatures, which is taken to be evidence for upwelling mantle beneath western Arabia (McGuire & Bohannon, 1989); (3) the initial ages of volcanism in western Arabia, indicating a northward propagation of the volcanic activity (Ershov & Nikishin, 2004). One component within the Afar mantle plume is reflected in Ethiopian lavas with high $^{3}He/^{4}He$ ratios (Marty *et al.*, 1996); however, this component has a much higher $^{87}Sr/^{86}Sr$ for a given $^{143}Nd/^{144}Nd$ and $^{206}Pb/^{204}Pb$ than the HAS lavas (Fig. 8b and g). Furthermore, the Ethiopian lavas have lower $^{206}Pb/^{204}Pb$ and $^{207}Pb/^{204}Pb$ compared with the HAS lavas. Thus, the Afar plume source with high $^{3}He/^{4}He$ does not appear to play a noticeable role in Syrian HAS volcanism; this is in agreement with the conclusions of Shaw *et al.* (2003). However, another mantle source with more radiogenic Pb isotopic compositions is represented in lavas from Afar, southwestern Arabia and from the oceanic crust in the Gulf of Aden (e.g. Schilling *et al.*, 1992; Baker *et al.*, 1996; Stewart & Rogers, 1996) (Fig. 8). The presence of this component beneath the HAS can explain the generation of the series I and III magmas; this component has been suggested to reside either in the Afar plume (Vidal *et al.*, 1991; Deniel *et al.*, 1994; Bertrand *et al.*, 2003) or to represent part of a plume head (Kieffer *et al.*, 2004) or to reflect the composition of the subcontinental lithosphere (Pik *et al.*, 1999; Bertrand *et al.*, 2003). However, in our opinion, the fact that this component also occurs in lavas erupting through oceanic lithosphere in the Gulf of Aden (Schilling *et al.*, 1992) rules out a continental lithospheric origin and we propose that this component must have a relatively high excess temperatures to explain the increased degree of melting at great pressure that produced the series III and I magmas. The repeated tapping of this source, before and after the eruption of the series II magmas, is difficult to explain by models involving lithospheric melting (Stein *et al.*, 1997; Bertrand *et al.*, 2003; Shaw *et al.*, 2003; Weinstein *et al.*, 2006), which typically yields the early magmas in continental rift regimes (e.g. DePaolo & Daley, 2000). Finally, the presence of relatively hot mantle material beneath large parts of Arabia is supported by the available geophysical data indicating a relatively low-velocity linear zone in the form of a pipe or channel at depths of 100–200 km extending from Ethiopia and Yemen through Saudi Arabia to Syria in the north (e.g. Debayle *et al.*, 2001; Daradich *et al.*, 2003; Ershov & Nikishin, 2004). Additionally, seismic tomography data do not support the presence of a separate mantle plume under northern Arabia as proposed by Camp & Roobol (1992). We suggest that this material is probably the mantle source component with high Pb isotope ratios from the Afar mantle plume.

Temporal variations of the HAS magmas

The variable fractionation-corrected major element compositions and REE ratios of the three HAS series, together with the ages of the lavas, suggest that mantle melting

processes must have varied considerably during the last 20 Myr underneath the HAS region (Figs 10 and 12). The variable degrees of melting observed in the source of the HAS lavas are probably due to a pulsing influx of mantle plume material from the Afar region in the south. Lateral plume flux has been proposed in the ocean basins, and the occurrence of V-shaped ridges along the Reykjanes spreading axis south of Iceland has been interpreted to reflect the pulsing of the Iceland plume (White *et al.*, 1995). Similarly, the inflowing plume material beneath the HAS may have been pulsing during the last 7 Myr with a decreasing influx between 3·5 and 1 Ma, when mainly asthenospheric material was the dominant source accounting for lower degrees of partial melting. The first period of volcanic activity (oldest series III lavas) occurred between 24 and 3·5 Ma. There was a major break in plume influx between 13 and 7 Ma, when no volcanic activity occurred in the northern HAS (Giannérini *et al.*, 1988; Mouty *et al.*, 1992; Sharkov *et al.*, 1994).

Variation in magma generation conditions over a shorter time period is evident in a stratigraphic section of lava flows sampled along the Wadi Ash-Sham, where lavas belonging to series II and III are exposed (Fig. 1c). These lava flows represent a temporal sequence in which the heights of the lavas above the base correlate with age. The $^{40}Ar/^{39}Ar$ ages for lavas from the lowermost and uppermost section are 4·2 Ma and 3·3 Ma, respectively (Table 4), suggesting that the about 700 m thick pile of lava erupted within about 900 kyr (Fig. 13). Except for two samples that have low $Si_{9.0}$ and variable $(La/Sm)_N$, generally suggesting low degrees of partial melting, the series III alkali basalts from the lower part of the section have high silica contents (45·9–47·0 wt %) accompanied by relatively low $(La/Sm)_N$ in the range of 1·78–2·69, thus reflecting relatively high degrees of partial melting (Fig. 13). Because most of the lavas show no evidence for crustal contamination, the increasing $(La/Sm)_N$ and decreasing $Si_{9.0}$ towards the top of the sequence indicate a decreasing degree of partial melting from series III to series II. This rapidly changing degree of melting within several hundred thousand years cannot be due to lithospheric thinning, but could be due to the variable influx of mantle with different temperatures and compositions as indicated by the distinct isotope compositions of the two series.

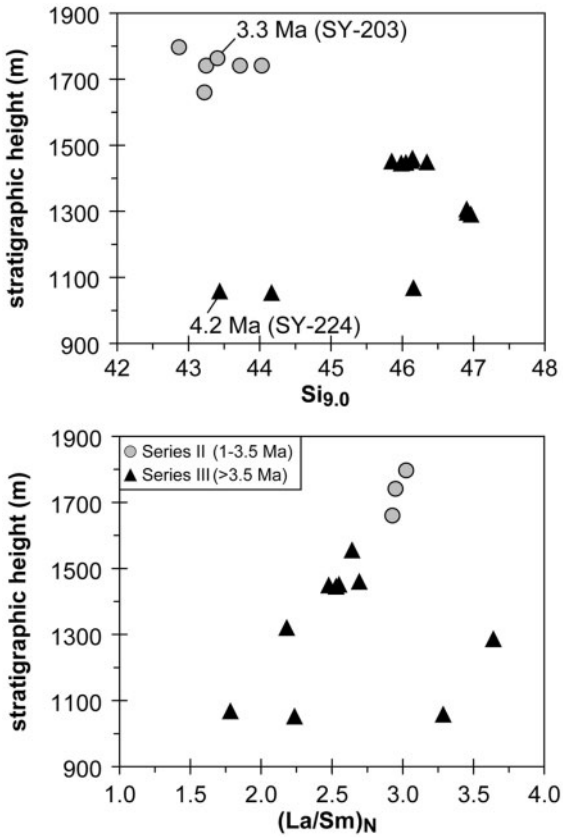

Fig. 13. Variations of $Si_{9.0}$ and $(La/Sm)_N$ vs stratigraphic height (metres) in the region of Wadi Ash-Sham (Fig. 1c). The $^{40}Ar/^{39}Ar$ ages of the samples are from this study and chondrite values are from McDonough & Sun (1995).

CONCLUSIONS

The investigation of the Miocene to recent lavas from the Harrat Ash Shamah volcanic field in southern Syria leads to the following conclusions.

(1) The lava suite comprises alkali basalts, basanites, tephrites, hawaiites, mugearites, rare trachytes and phonolites.

(2) The major and compatible trace element composition of the lavas is controlled by the fractional crystallization of olivine, clinopyroxene, ± Fe–Ti oxides.

(3) The major element chemistry of the highly differentiated lavas is additionally controlled by apatite and minor feldspar fractionation.

(4) Some rocks have been affected by olivine accumulation as shown by their high Ni concentrations and high Ni/Cr ratios.

(5) The low Ce/Pb (15·9–5·99) and Nb/U (34·6–22·0) and high K/La (>350) ratios as well as the high $^{87}Sr/^{86}Sr$ (>0·7039) and low $^{143}Nd/^{144}Nd$ (<0·5216) ratios displayed by a number of samples indicate the assimilation of continental crustal material.

(6) The major element variations and the variably fractionated HREE ratios of the uncontaminated, primitive lavas could be produced by different degrees of partial melting of garnet peridotite mantle sources at depths of about 100 km.

(7) As indicated by the isotopic and incompatible trace element ratios, the parental magmas of the Harrat Ash

Shamah volcanic field are derived from volatile- and incompatible element-enriched asthenosphere and plume mantle sources.

(8) The discontinuous volcanism found throughout the HAS volcanic field in conjunction with the temporal variations of lava composition and melting regime are consistent with the activity of a pulsing mantle plume underneath southern Syria that can be related to the Afar mantle plume.

ACKNOWLEDGEMENTS

The 'field team' is deeply indebted to the University of Aleppo for the support in Syria. H. Blaschek, D. Garbe-Schönberg and K. Kißling are thanked for help with the ICP-MS analyses. P. Appel, H. Baier, F. Hauff, S. Hauff, B. Mader, P. Rengers, P. van den Bogaard and A. Weinkauf are acknowledged for their help during analytical work. M.-S.K. would like to thank N.A. Stroncik for helpful comments on an earlier version of the manuscript. The constructive reviews and comments by N.W. Rogers, J. Baker, Y. Weinstein and the editor M. Wilson helped to improve the manuscript significantly. This study was funded by the Deutsche Forschungsgemeinschaft (grant HA 2568/5) and is part of M.-S.K.'s dissertation.

REFERENCES

Albarède, F. (1992). How deep do common basaltic magmas form and differentiate? *Journal of Geophysical Research* **97**, 10997–11009.

Al-Damegh, K., Sandvol, E. & Barazangi, M. (2005). Crustal structure of the Arabian plate: New constraints from the analysis of teleseismic receiver functions. *Earth and Planetary Science Letters* **231**, 177–196; doi: 110.1016/j.epsl.2004.1012.1020.

Almond, D. C. (1986). Geological evolution of the Afro-Arabian Dome. *Tectonophysics* **131**, 301–332.

Altherr, R., Henjes-Kunst, F. & Baumann, A. (1990). Asthenosphere versus lithosphere as possible sources for basaltic magmas erupted during formation of the Red Sea; constraints from Sr, Pb and Nd isotopes. *Earth and Planetary Science Letters* **96**, 269–286.

Baker, J. A., Thirlwall, M. F. & Menzies, M. A. (1996). Sr–Nd–Pb isotopic and trace element evidence for crustal contamination of plume-derived flood basalts; Oligocene flood volcanism in western Yemen. *Geochimica et Cosmochimica Acta* **60**, 2559–2581.

Baker, J. A., Macpherson, C. G., Menzies, M. A., Thirlwall, M. F., Al Kadasi, M. & Mattey, D. P. (2000). Resolving crustal and mantle contributions to continental flood volcanism, Yemen; constraints from mineral oxygen isotope data. *Journal of Petrology* **41**, 1805–1820.

Barberi, F., Capaldi, G., Gasperini, P., Marinelli, G., Santacroce, R., Scandone, R., Treuil, M. & Varet, J. (1980). Recent basaltic volcanism of Jordan and its implications on the geodynamic history of the Dead Sea shear zone. In: Carrelli, A. (ed.) *Geodynamic Evolution of the Afro-Arabian Rift System*. Rome: Accademia Nazionale dei Lincei, pp. 667–683.

Bertrand, H., Chazot, G., Blichert-Toft, J. & Thoral, S. (2003). Implications of widespread high-μ volcanism on the Arabian Plate for Afar mantle plume and lithosphere composition. *Chemical Geology* **198**, 47–61.

Best, J. A., Barazangi, M., Al Saad, D., Sawaf, T. & Gebran, A. (1990). Bouguer gravity trends and crustal structure of the Palmyride mountain belt and surrounding northern Arabian Platform in Syria. *Geology* **18**, 1235–1239.

Brew, G., Barazangi, M., Sawaf, T. & Al-Maleh, K. (2000). Tectonic map and geologic evolution of Syria: The role of GIS. *Leading Edge* **19**, 176–182.

Brew, G., Barazangi, M., Al-Maleh, A. K. & Sawaf, T. (2001a). Tectonic and geologic evolution of Syria. *GeoArabia* **6**, 573–616.

Brew, G., Lupa, J., Barazangi, M., Sawaf, T., Al-Imam, A. & Zaza, T. (2001b). Structure and tectonic development of the Ghab basin and the Dead Sea fault system, Syria. *Journal of the Geological Society, London* **158**, 665–674.

Camp, V. E. & Roobol, M. J. (1992). Upwelling asthenosphere beneath western Arabia and its regional implications. *Journal of Geophysical Research* **97**, 15255–15271.

Campbell, I. H. & Griffiths, R. W. (1990). Implications of mantle plume structure for the evolution of flood basalts. *Earth and Planetary Science Letters* **99**, 79–93.

Coleman, R. G., Gregory, R. T. & Brown, G. F. (1983). Cenozoic volcanic rocks of Saudi Arabia. *US Geological Survey, Open-File Report* **OF 83-0788**, 86.

Daradich, A., Mitrovica, J. X., Pysklywec, R. N., Willett, S. D. & Forte, A. M. (2003). Mantle flow, dynamic topography, and rift-flank uplift of Arabia. *Geology* **31**, 901–904.

Debayle, E., Leveque, J. J. & Cara, M. (2001). Seismic evidence for a deeply rooted low-velocity anomaly in the upper mantle beneath the northeastern Afro/Arabian continent. *Earth and Planetary Science Letters* **193**, 423–436.

Deniel, C., Vidal, P., Coulon, C., Vellutini, P.-J. & Piguet, P. (1994). Temporal evolution of mantle sources during continental rifting: The volcanism of Djibouti (Afar). *Journal of Geophysical Research* **99**, 2853–2869.

DePaolo, D. J. & Daley, E. E. (2000). Neodymium isotopes in basalts of the southwest Basin and Range and lithospheric thinning during continental extension. *Chemical Geology* **169**, 157–185.

Duffield, W. A. & Dalrymple, G. B. (1990). The Taylor Creek Rhyolite of New Mexico; a rapidly emplaced field of lava domes and flows. *Bulletin of Volcanology* **52**, 475–487.

Eggler, D. H. (1978). The effect of CO_2 upon partial melting of peridotite in the system Na_2O–CaO–Al_2O_3–MgO–SiO_2–CO_2 to 35 kb, with an analysis of melting in a peridotite–H_2O–CO_2 system. *American Journal of Science* **278**, 305–343.

Eissen, J. P., Juteau, T., Joron, J. L., Dupré, B., Humler, E. & Al'Mukhamedov, A. (1989). Petrology and geochemistry of basalts from the Red Sea axial rift at 18 degrees North. *Journal of Petrology* **30**, 791–839.

El-Isa, Z. H., Mechie, J., Prodehl, C., Makris, J. & Rihm, R. (1987). A crustal structure study of Jordan derived from seismic refraction data. *Tectonophysics* **138**, 235–253.

Ershov, A. V. & Nikishin, A. M. (2004). Recent geodynamics of the Caucasus–Arabia–East Africa region. *Geotectonics* **38**, 123–136.

Falloon, T. J. & Green, D. H. (1990). Solidus of carbonated fertile peridotite under fluid-saturated conditions. *Geology* **18**, 195–199.

Gallagher, K. & Hawkesworth, C. J. (1992). Dehydration melting and the generation of continental flood basalts. *Nature* **358**, 57–59.

Garbe-Schönberg, C.-D. (1993). Simultaneous determination of thirty-seven trace elements in twenty-eight international rock standards by ICP-MS. *Geostandards Newsletter* **17**, 81–97.

Giannérini, G., Campredon, R., Féraud, G. & Abou Zakhem, B. (1988). Déformations intraplaques et volcanisme associé; exemple de la bordure NW de la plaque Arabique au Cenozoique. *Bulletin de la Société Géologique de France, Huitieme Série* **4**, 937–947.

Green, D. H. (1973). Experimental melting studies on a model upper mantle composition at high pressure under water-saturated and water-undersaturated conditions. *Earth and Planetary Science Letters* **19**, 37–53.

Guba, I. & Mustafa, H. (1988). Structural control of young basaltic fissure eruptions in the plateau basalt area of the Arabian Plate, northeastern Jordan. *Journal of Volcanology and Geothermal Research* **35**, 319–334.

Haase, K. M. (1996). The relationship between the age of the lithosphere and the composition of oceanic magmas; constraints on partial melting, mantle sources and the thermal structure of the plates. *Earth and Planetary Science Letters* **144**, 75–92.

Haase, K. M., Muehe, R. & Stoffers, P. (2000). Magmatism during extension of the lithosphere; geochemical constraints from lavas of the Shaban Deep, northern Red Sea. *Chemical Geology* **166**, 225–239.

Hart, S. R. & Dunn, T. (1993). Experimental cpx/melt partitioning of 24 trace elements. *Contributions to Mineralogy and Petrology* **113**, 1–8.

Hegner, E. & Pallister, J. S. (1989). Pb, Sr, and Nd isotopic characteristics of Tertiary Red Sea Rift volcanics from the central Saudi Arabian coastal plain. *Journal of Geophysical Research* **94**, 7749–7755.

Heimann, A. & Ron, H. (1993). Geometric changes of plate boundaries along part of the northern Dead Sea Transform; geochronologic and paleomagnetic evidence. *Tectonics* **12**, 477–491.

Heimann, A., Steinitz, G., Mor, D. & Shaliv, G. (1996). The Cover Basalt Formation, its age and its regional and tectonic setting; implications from K–Ar and $^{40}Ar/^{39}Ar$ geochronology. *Israel Journal of Earth-Sciences* **45**, 55–71.

Hirose, K. (1997). Partial melt compositions of carbonated peridotite at 3 GPa and role of CO_2 in alkali-basalt magma generation. *Geophysical Research Letters* **24**, 2837–2840.

Hirose, K. & Kushiro, I. (1993). Partial melting of dry peridotites at high pressures; determination of compositions of melts segregated from peridotite using aggregates of diamond. *Earth and Planetary Science Letters* **114**, 477–489.

Hofmann, A. W., Jochum, K. P., Seufert, M. & White, W. M. (1986). Nb and Pb in oceanic basalts; new constraints on mantle evolution. *Earth and Planetary Science Letters* **79**, 33–45.

Ilani, S., Harlavan, Y., Tarawneh, K., Rabba, I., Weinberger, R., Ibrahim, K., Peltz, S. & Steinitz, G. (2001). New K–Ar ages of basalts from the Harrat Ash Shaam volcanic field in Jordan: Implications for the span and duration of the upper-mantle upwelling beneath the western Arabian plate. *Geology* **29**, 171–174.

Jarrar, G., Stern, R. J., Saffarini, G. & Al-Zubi, H. (2003). Late- and post-orogenic Neoproterozoic intrusions of Jordan: implications for crustal growth in the northernmost segment of the East African Orogen. *Precambrian Reseach* **123**, 295–319.

Johnson, K. T. M. (1998). Experimental determination of partition coefficients for rare earth and high-field-strength elements between clinopyroxene, garnet, and basaltic melt at high pressure. *Contributions to Mineralogy and Petrology* **133**, 60–68.

Kelemen, P. B., Shimizu, N. & Dunn, T. (1993). Relative depletion of niobium in some arc magmas and the continental crust; partitioning of K, Nb, La and Ce during melt/rock reaction in the upper mantle. *Earth and Planetary Science Letters* **120**, 111–133.

Kieffer, B., Arndt, N., Lapierre, H., Bastien, F., Bosch, D., Pecher, A., Yirgu, G., Ayalew, D., Weis, D., Jerram, D. A., Keller, F. & Meugniot, C. (2004). Flood and shield basalts fromEthiopia: magmas from the African Superswell. *Journal of Petrology* **45**, 793–834; doi: 10.1093/petrology/egg1112.

Klein, E. M. & Langmuir, C. H. (1987). Global correlations of ocean ridge basalt chemistry with axial depth and crustal thickness. *Journal of Geophysical Research* **92**, 8089–8115.

Le Bas, M. J., Le Maitre, R. W., Streckeisen, A. & Zanettin, B. A. (1986). Chemical classification of volcanic rocks based on the total alkali–silica diagram. *Journal of Petrology* **27**, 745–750.

Leeman, W. P. & Scheidegger, K. F. (1977). Olivine/liquid distribution coefficients and a test for crystal–liquid equilibrium. *Earth and Planetary Science Letters* **35**, 247–257.

MacDonald, G. A. (1968). Composition and origin of Hawaiian lavas. In: Coats, R. R., Hay, R. L. & Anderson, C. A. (eds.) *Studies in Volcanology: A Memoir in Honour of Howel Wiliams,* Geological Society of America, Memoirs **116**, 477–522.

Marty, B., Pik, R. & Gezahegn, Y. (1996). Helium isotopic variations in Ethiopian plume lavas; nature of magmatic sources and limit on lower mantle contribution. *Earth and Planetary Science Letters* **144**, 223–237.

McBride, J. H., Barazangi, M., Best, J., Al Saad, D., Sawaf, T., Al Otri, M. & Gebran, A. (1990). Seismic reflection structure of intracratonic Palmyride fold–thrust belt and surrounding Arabian Platform, Syria. *AAPG Bulletin* **74**, 238–259.

McDonough, W. F. & Sun, S.-s. (1995). The composition of the Earth. *Chemical Geology* **120**, 223–253.

McGuire, A. V. & Bohannon, R. G. (1989). Timing of mantle upwelling; evidence for a passive origin for the Red Sea Rift. *Journal of Geophysical Research* **94**, 1677–1682.

McKenzie, D. & Bickle, M. J. (1988). The volume and composition of melt generated by extension of the lithosphere. *Journal of Petrology* **29**, 625–679.

Mohsen, A., Kind, R., Sobolev, S. V., Weber, M. & Group, D. (2006). Thickness of the lithosphere east of the Dead Sea Transform. *Geophysical Journal International* **167**, 845–852.

Mor, D. (1993). A time-table for the Levant volcanic province, according to K–Ar dating in the Golan Heights, Israel. *Journal of African Earth Sciences* **16**, 223–234.

Mouty, M., Delaloye, M., Fontignie, D., Piskin, O. & Wagner, J. J. (1992). The volcanic activity in Syria and Lebanon between Jurassic and Actual. *Schweizerische Mineralogische und Petrographische Mitteilungen* **72**, 91–105.

Mysen, B. O. & Kushiro, I. (1977). Compositional variations of coexisting phases with degree of melting of peridotite in the upper mantle. *American Mineralogist* **62**, 843–865.

Nasir, S. (1992). The lithosphere beneath the northwestern part of the Arabian Plate (Jordan); evidence from xenoliths and geophysics. *Tectonophysics* **201**, 357–370.

Nasir, S. (1994). Geochemistry and petrogenesis of Cenozoic volcanic rocks from the northwestern part of the Arabian continental alkali basalt province, Jordan. *Africa Geoscience Review* **1**, 455–467.

Nasir, S. (1995). Mafic lower crustal xenoliths from the northwestern part of the Arabian Plate. *European Journal of Mineralogy* **7**, 217–230.

Nasir, S. & Safarjalani, A. (2000). Lithospheric petrology beneath the northern part of the Arabian Plate in Syria: evidence from xenoliths in alkali basalts. *Journal of African Earth Sciences* **30**, 149–168.

Onuma, N., Higuchi, H., Wakita, H. & Nagasawa, H. (1968). Trace element partition between two pyroxenes and the host lava. *Earth and Planetary Science Letters* **5**, 47–51.

Pik, R., Deniel, C., Coulon, C., Yirgu, G. & Marty, B. (1999). Isotopic and trace element signatures of Ethiopian flood basalts; evidence for plume–lithosphere interactions. *Geochimica et Cosmochimica Acta* **63**, 2263–2279.

Ponikarov, V. P. (1969). *Syria.* Moscow: Nedra (in Russian).

Ponikarov, V. P., Protasevich, L., Maximov, A. & Tkachev, G. (1963). *Geological Map of Syria, 1:200 000.* Moscow: V.O. Technoexport.

Robinson, J. A. C. & Wood, B. J. (1998). The depth of the spinel to garnet transition at the peridotite solidus. *Earth and Planetary Science Letters* **164**, 277–284.

Rogers, N. W. (1993). The isotope and trace element geochemistry of basalts from the volcanic islands of the southern Red Sea. *Journal of the Geological Society, London* **76**, 455–467.

Rudnick, R. L. & Fountain, D. M. (1995). Nature and composition of the continental crust; a lower crustal perspective. *Reviews of Geophysics* **33**, 267–309.

Scarrow, J. H. & Cox, K. G. (1995). Basalts generated by decompressive adiabatic melting of a mantle plume; a case study from the Isle of Skye, NW Scotland. *Journal of Petrology* **36**, 3–22.

Schilling, J. G. (1973). Afar mantle plume: Rare earth evidence. *Nature* **242**, 2–5.

Schilling, J. G., Kingsley, R. H., Hanan, B. B. & McCully, B. L. (1992). Nd–Sr–Pb isotopic variations along the Gulf of Aden; evidence for Afar mantle plume–continental lithosphere interaction. *Journal of Geophysical Research* **97**, 10927–10966.

Sengör, A. M. C. & Burke, K. (1978). Relative timing of rifting and volcanism on Earth and its tectonic implications. *Geophysical Research Letters* **5**, 419–421.

Sharkov, Y. V., Lazko, Y. Y., Fedosova, S. P. & Hanna, S. (1989). Depth-derived inclusions of the Quaternary volcano Tèl-Danun, southern Syria, in relation to the problem of intraplate basaltic magmatism. *Geokhimiya* **11**, 1609–1623 (in Russian).

Sharkov, Y. V., Chernyshev, I. V., Devyatkin, Y. V., Dodonov, A. Y., Ivanenko, V. V., Karpenko, M. I., Leonov, Y. G., Novikov, V. M., Khanna, S. & Khatib, K. (1994). Geochronology of late Cenozoic basalts in western Syria. *Petrologiya* **2**, 385–394 (in Russian).

Shaw, J. E., Baker, J. A., Menzies, M. A., Thirlwall, M. F. & Ibrahim, K. M. (2003). Petrogenesis of the largest intraplate volcanic field on the Arabian Plate (Jordan): a mixed lithosphere–asthenosphere source activated by lithospheric extension. *Journal of Petrology* **44**, 1657–1679.

Snyder, G. A., Taylor, L. A., Jerde, E. A., Sharkov, Y., Laz, K. Y. & Hanna, S. (1993). Petrogenesis of garnet pyroxenite and spinel peridotite xenoliths of the Tèll-Danun alkali basalt volcano, Harrat as Shamah, Syria. *International Geology Review* **35**, 1104–1120.

Steiger, R. H. & Jäger, E. (1977). Subcommission on geochronology; convention on the use of decay constants in geo- and cosmochronology. *Earth and Planetary Science Letters* **36**, 359–362.

Stein, M. & Hofmann, A. W. (1992). Fossil plume head beneath the Arabian lithosphere? *Earth and Planetary Science Letters* **114**, 193–209.

Stein, M., Navon, O. & Kessel, R. (1997). Chromatographic metasomatism of the Arabian–Nubian lithosphere. *Earth and Planetary Science Letters* **152**, 75–91.

Stewart, K. & Rogers, N. (1996). Mantle plume and lithosphere contributions to basalts from southern Ethiopia. *Earth and Planetary Science Letters* **139**, 195–211.

Sun, S. S. & McDonough, W. F. (1989). Chemical and isotopic systematics of oceanic basalts; implications for mantle composition and processes. In: Saunders, A. D. & Norry, M. J. (eds) *Magmatism in the Ocean Basins. Geological Society, London, Special Publications* **42**, 313–345.

Suzuki, T., Akaogi, M. & Nakamura, E. (2000). Partitioning of major elements between garnet-structured minerals and silicate melt at pressure of 3–15 GPa. *Physics of the Earth and Planetary Interiors* **120**, 79–92.

Tarawneh, K., Ilani, S., Rabba, I., Harlavan, Y., Peltz, S., Ibrahim, K., Weinberger, R. & Steinitz, G. (2000). Dating of the Harrat Ash Shaam Basalts Northeast Jordan (Phase 1). *Hashemite Kingdom of Jordan, Natural Resources Authority; Geological Survey of Israel Report GSI/2/2000*, 59 pp.

Taylor, J. R. (1982). *An Introduction to Error Analysis*. Mill Valley, CA: University Science Books.

Turner, S., Hawkesworth, C., Gallagher, K., Stewart, K., Peate, D. & Mantovani, M. (1996). Mantle plumes, flood basalts, and thermal models for melt generation beneath continents: Assessment of a conductive heating model and application to the Parana. *Journal of Geophysical Research* **101**, 11503–11518.

Vidal, P., Deniel, C., Vellutini, P. J., Piguet, P., Coulon, C., Vincent, J. & Audin, J. (1991). Changes of mantle sources in the course of a rift evolution: The Afar case. *Geophysical Research Letters* **18**, 1913–1916.

Wallace, M. E. & Green, D. H. (1988). An experimental determination of primary carbonatite magma composition. *Nature* **335**, 343–346.

Weinstein, Y. (2000). Spatial and temporal geochemical variability in basin-related volcanism, northern Israel. *Journal of African Earth Sciences* **30**, 865–886.

Weinstein, Y., Navon, O., Altherr, R. & Stein, M. (2006). The role of lithospheric mantle heterogeneity in the generation of Plio-Pleistocene alkali basaltic suites from NW Harrat Ash Shaam (Israel). *Journal of Petrology* **47**, 1017–1050; doi:10.1093/petrology/egl1003.

White, R. & McKenzie, D. (1989). Magmatism at rift zones; the generation of volcanic continental margins and flood basalts. In: Leeman, W. P. & Fitton, J. G. (eds) *Special Section on Magmatism Associated with Lithospheric Extension*. Washington, DC: American Geophysical Union, pp. 7685–7729.

White, R. S., Bown, J. W. & Smallwood, J. R. (1995). The temperature of the Iceland plume and origin of outward-propagating V-shaped ridges. *Journal of the Geological Society, London* **152**, 1039–1045.

Wyllie, P. J. (1978). Mantle fluid compositions buffered in peridotite–CO_2–H_2O by carbonates, amphibole, and phlogopite. *Journal of Geology* **86**, 687–713.

York, D. (1969). Least squares fitting of a straight line with correlated errors. *Earth and Planetary Science Letters* **5**, 320–324.

Ziegler, P. A. & Cloetingh, S. (2004). Dynamic processes controlling evolution of rifted basins. *Earth-Science Reviews* **64**, 1–50.